Research article

JGS
Journal of the Geological Society

Published online June 11, 2020

https://doi.org/10.1144/jgs2019-199 | Vol. 177 | 2020 | pp. 965–980

The Atud gabbro–diorite complex: glimpse of the Cryogenian mixing, assimilation, storage and homogenization zone beneath the Eastern Desert of Egypt

Robert J. Stern[1], Kamal Ali[2], Paul D. Asimow[3], Mokhles K. Azer[4], Matthew I. Leybourne[5], Heba S. Mubarak[4], Minghua Ren[6], Rolf L. Romer[7] and Martin J. Whitehouse[8]

[1] Geosciences Department, University of Texas at Dallas, Richardson, TX 75083-0688, USA
[2] United Arab Emirates University, Geology Department, PO Box 15551, Al Ain, Abu Dhabi, UAE
[3] Division of Geological and Planetary Sciences, California Institute of Technology, Pasadena, CA 91125, USA
[4] Geological Sciences Department, National Research Centre, Cairo, Egypt
[5] Queen's Facility for Isotope Research, Department of Geological Sciences and Geological Engineering, Queen's University, Kingston, ON K7L 3N6, Canada
[6] Department of Geoscience, University of Nevada Las Vegas, NV 89154, USA
[7] GFZ German Research Centre for Geosciences, Telegrafenberg, D-14473 Potsdam, Germany
[8] Department of Geosciences, Swedish Museum of Natural History, SE-104 05 Stockholm, Sweden

RJS, 0000-0002-8083-4632; KA, 0000-0002-7332-7843; PDA, 0000-0001-6025-8925; MKA, 0000-0002-3711-8630; MJW, 0000-0003-2227-577X

Correspondence: rjstern@utdallas.edu

Abstract: We analysed gabbroic and dioritic rocks from the Atud igneous complex in the Eastern Desert of Egypt to understand better the formation of juvenile continental crust of the Arabian–Nubian Shield. Our results show that the rocks are the same age (U–Pb zircon ages of 694.5 ± 2.1 Ma for two diorites and 695.3 ± 3.4 Ma for one gabbronorite). These are partial melts of the mantle and related fractionates (εNd_{690} = +4.2 to +7.3, $^{87}Sr/^{86}Sr_i$ = 0.70246–0.70268, zircon $\delta^{18}O \sim +5‰$). Trace element patterns indicate that Atud magmas formed above a subduction zone as part of a large and long-lived (*c*. 60 myr) convergent margin. Atud complex igneous rocks belong to a larger metagabbro–epidiorite–diorite complex that formed as a deep crustal mush into which new pulses of mafic magma were periodically emplaced, incorporated and evolved. The petrological evolution can be explained by fractional crystallization of mafic magma plus variable plagioclase accumulation in a mid- to lower crustal MASH zone. The Atud igneous complex shows that mantle partial melting and fractional crystallization and plagioclase accumulation were important for Cryogenian crust formation in this part of the Arabian–Nubian Shield.

Supplementary material: Analytical methods and data, calculated equilibrium mineral temperatures, results of petrogenetic modeling, and cathodluminesence images of zircons can be found at https://doi.org/10.6084/m9.figshare.c.4958822

Received 2 December 2019; **revised** 28 April 2020; **accepted** 30 April 2020

Neoproterozoic crust of the Arabian–Nubian Shield is beautifully exposed in the rift-flank uplift around the Red Sea, including the Eastern Desert of Egypt. Eastern Desert crust formed *c*. 800–580 Ma during the protracted Pan-African orogenic cycle and consists of juvenile continental crust (Stern 2017). This Eastern Desert crustal tract has long been regarded as an outstanding example of how continental crust is produced by plate-tectonic processes (Engel *et al.* 1980; Stern 2017). We have much to learn about how this crust was produced, especially unravelling the role of mantle partial melts and how these were processed in the crust to yield juvenile continental crust. To do this, we need to understand better the composition of mafic magmas and how these evolved in the lower and middle crust. Much of this processing happens in what are called MASH zones, where mafic melts from the mantle are Mixed, Assimilated, Stored, and Homogenized (Hildreth and Moorbath 1988). Small-scale (few km^2) intrusions can provide natural laboratories for reconstructing these processes. The results we present here concern a small mafic intrusion and what it tells us about the evolution of the crust of this region.

The Atud gabbro–diorite intrusion is a small (few km^2) Neoproterozoic plutonic body in the Eastern Desert of Egypt (Figs 1 and 2) that provides key insights into Neoproterozoic mafic igneous activity and thus how the crust of Egypt formed. The Atud body intruded deformed Cryogenian–Tonian ophiolites and island-arc assemblages but is itself undeformed; for this reason, it is sometimes thought to be a post-orogenic intrusion. The Atud intrusion has been the focus of study for several decades yet its significance in the crustal evolution of this part of the Arabian–Nubian Shield remains unclear, partly because its age is unknown and partly because it has not been systematically studied with a full suite of modern analytical tools. Akaad and Essawy (1964) related the Atud intrusion to the enigmatic epidiorite–diorite complex of the Central Eastern Desert, also known as the metagabbro–diorite complex; for simplicity we call this the metagabbro epidiorite–diorite (MED) complex. Akaad and Essawy (1964) thought that the Atud intrusion defined the southern periphery of the MED complex (Fig. 1b). In contrast, El Ramly (1972) interpreted the Atud gabbro as a post-Hammamat (Ediacaran or younger) post-tectonic intrusion. We need to know more about the Atud gabbro–diorite intrusion and its relationship to the MED complex, which may represent a Cryogenian MASH zone. The intrusion is a natural place to begin this effort because its gold deposits are also important to economic geologists (Abdelnasser and Kumral 2017). Here we report the results of a modern petrographic, mineral chemistry,

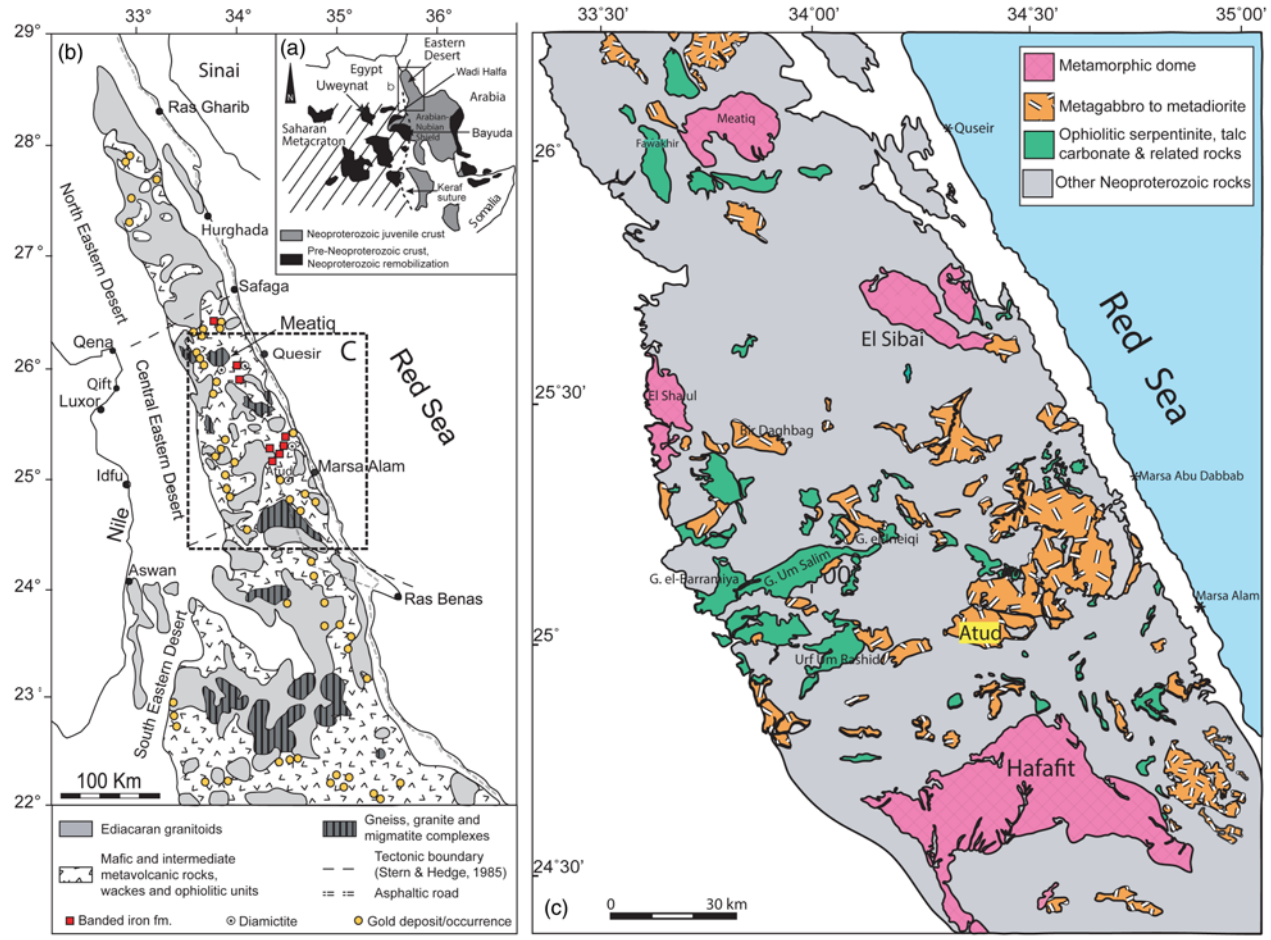

Fig. 1. Geological setting of the study area (Red Sea is closed). (**a**) Regional setting showing location of Arabian–Nubian Shield (juvenile Neoproterozoic crust) and flanking older crust. (**b**) Simplified geological map of the Eastern Desert of Egypt (modified from Stern and Hedge 1985) showing the BIF–diamictite occurrences and gold deposits. Location of (**c**) is also shown. (**c**) Geological map for the Central Eastern Desert of Egypt showing the distribution of metagabbro and metadiorite and other Neoproterozoic basement rocks (modified from CONOCO 1:500 000 map and compiled from two quadrangle maps: Quseir quadrangle NG 36 NE and Gabal Hamata quadrangle NG 36 SE (General Petroleum Corporation 1987)). Distribution of the metagabbro–epidiorite–diorite (MED) complex overlaps with distribution of metagabbros and metadiorites.

whole-rock major and trace element and radiogenic isotopic, and U–Pb zircon geochronological study. We show that the Atud intrusion, and by implication the MED complex, reflects massive addition of melt from subduction-modified juvenile mantle to the crust that occurred *c*. 700 Ma.

Geological setting

There are two types of gabbro recognized in the Central Eastern Desert (Ghoneim 1989): the older Sid Metagabbros, which include all of the metamorphosed gabbros (e.g. metagabbro, amphibolite and gneissose metagabbro) and the Younger Gabbro, which is younger and shows less metamorphic overprint. Both groups are probably components of multiple phases of igneous activity, as shown by Figure 3 (our results place the Atud complex at the beginning of Eastern Desert igneous activity). The Atud gabbro is exposed as a *c*. 3 km × 3 km intrusion into metasedimentary and ophiolitic rocks. The eastern half of the intrusion is dioritic and the western half is gabbroic (Fig. 2). One key question is the relationship between gabbro and hornblende diorite, neither of which has previously been radiometrically dated. The hornblende diorite is much more altered than the gabbro, hosts the gold mineralization and is generally thought to be significantly older. Abdelnasser and Kumral (2017) stated that the Atud gabbro–diorite intrusion reflects calc-alkaline magmas, which intruded older ophiolites and island-arc assemblages. They assigned the altered diorites to the metagabbro–diorite complex and inferred that older diorites were intruded by olivine gabbro. However, there is no clear intrusive contact and the two suites share some common features, especially the presence of magmatic hornblende. Our geochronological data indicate that gabbroic and dioritic rocks are approximately the same age, *c*. 700 Ma, and thus are parts of a single magmatic complex.

Methods

Thirteen samples were studied petrographically, then subjected to electron microprobe mineral analysis (EMPA), whole-rock geochemical analyses, whole-rock Sr–Nd–Pb isotopic analyses and U–Pb zircon geochronological studies. Analytical details are presented in Supplementary Document 1. A subset was selected for electron microprobe studies, which were carried out at the University of Nevada, Las Vegas. EMPA mineral analyses (olivine, orthopyroxene, clinopyroxene, plagioclase, amphibole, chlorite, epidote, sepiolite, titanite, ilmenite and mica) are presented in Supplementary Table 1a–k. Whole-rock geochemical analyses were carried out at ALS Geochemistry, Vancouver, BC, Canada and are reported in Supplementary Table 2; International Geo Sample Numbers (IGSNs) for these samples can also be found in this table. Zircon U–Pb dating and O isotopic analyses were carried out in the NordSIMS lab in Stockholm, Sweden and are reported in Supplementary Tables 3 and 4, respectively. Ages and age

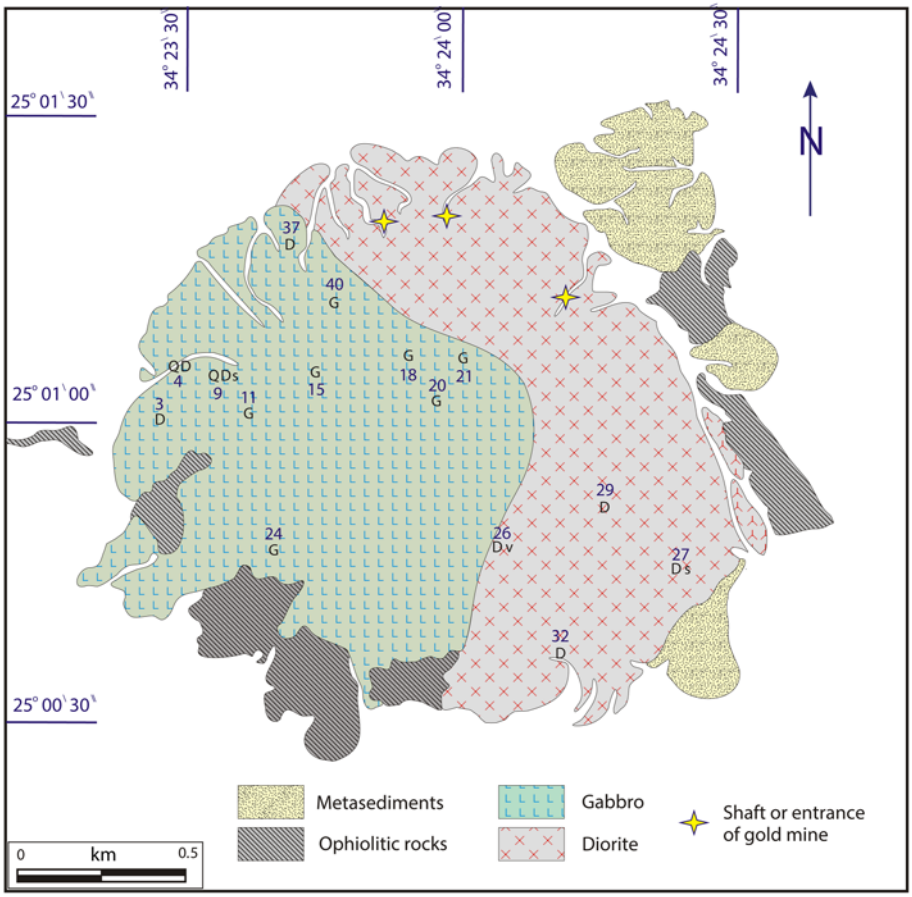

Fig. 2. Simplified geological map of the Atud intrusion showing location of studied samples. Letters indicate lithologies and numbers indicate sample numbers. G, gabbro; D, diorite; QD, quartz diorite; v, very altered; s, slightly altered. Sample numbers omit prefixes; for example, '9' on map corresponds to 'AT9' in Supplementary Table 2.

uncertainties calculated following Ludwig (2001). Strontium, Nd and Pb isotopic analyses were conducted at GFZ, Potsdam, Germany, and are reported in Supplementary Table 5. Calculated equilibrium mineral temperatures are reported in Supplementary Table 6.

Petrography, mineral chemistry and mineral equilibation temperatures

Atud complex igneous rocks can be divided on a basis of modal composition into gabbroic (Fig. 4a) and dioritic (Fig. 4b) rocks. Dioritic samples come from the eastern exposures and the lower slopes on the NW flank of Gebel Atud; gabbroic samples come from the upper slopes and southern flank, suggesting that relationships are more complicated than shown in Figure 2. Although mineral layering is not well developed, overall the gabbroic samples have the appearance of cumulate rocks (Fig. 5a), composed of olivine, plagioclase, clinopyroxene, orthopyroxene, opaque minerals and patchy interstitial hornblende. The rocks are phaneritic, with grain sizes of a few millimetres (Fig. 5c and d). Olivine crystals are large (up to a few millimetres) but embayed and generally rimmed with orthopyroxene (Fig. 5e), indicating disequilibrium. Large plagioclase crystals are euhedral and unzoned, although more sodic crystals are found in interstices. The presence of hornblende and orthopyroxene in the gabbronorite is a link with the diorites, suggesting that gabbroic and dioritic rocks formed as less and more differentiated equivalents that are broadly similar in age.

All seven mafic samples are generally unaltered and broadly gabbronorites that contain olivine, orthopyroxene, clinopyroxene, plagioclase and amphibole, with minor pyrite (some have chalcopyrite coexisting with pyrite) and apatite (Fig. 5e and f). Lithologies range from hornblende olivine gabbronorite to hornblende olivine gabbro and hornblende olivine leucogabbro (Fig. 4a). In the gabbroic rocks, modal proportions of olivine (OL) range from 5 to 18%, orthopyroxene (OPX) from 5 to 10%, clinopyroxene (CPX) from 15 to 31%, plagioclase (PL) from 35 to 61%, and hornblende (HB) from 3 to 15%. OL is anhedral with altered rims and rare fractures. The alteration phases are chlorite and an unidentified alteration product of olivine, perhaps a mixture of sepiolite and serpentine. OPX forms rims on OL as well as individual grains. CPX is anhedral, fills interstices between PL and rarely contains PL with ophitic (poikilitic) texture. Some CPX has been altered to amphibole; some amphiboles contain rounded CPX relict cores. PL typically has subhedral lath habit that rarely shows parallel alignment.

Dioritic rocks can be subdivided on a basis of modal quartz contents into diorites and quartz diorites (Fig. 4b). Diorites (AT27, 32 and 37) contain relics of CPX and calcic PL. Diorite AT29 is highly altered and is composed of epidote, chlorite and albite. Diorite AT32 plagioclase has large cores of $An_{75–85}$ surrounded by thin rims of $An_{55–56}$. Some plagioclase cores have been altered to epidote with albite-rich plagioclase ($An_{20–25}$). Quartz diorites (AT3, 4 and 9) contain few relict minerals. In sample AT3, amphibole is zoned and is locally altered to chlorite. Plagioclase cores are altered to epidote plus albitic plagioclase and are associated with $An_{10–30}$ rims. Sample AT9 contains zoned plagioclase, with labradorite ($An_{52–55}$) cores surrounded by oligoclase ($An_{9–19}$) rims. Cores are partly altered to prehnite–epidote and albite. Quartz is interstitial to plagioclase.

Compositions of pyroxene, olivine and plagioclase for gabbroic rocks are summarized in Figure 6a–c. Compositions of plagioclase for dioritic rocks are summarized in Figure 6d. Compositions of amphiboles for both suites are shown in Figure 6e. Based on OL and OPX compositions (Fig. 6a and b), AT11 and AT15 are similar, with more Mg-rich OL and OPX. AT15, 18, 20, 21 and 40 have similar chemistry; their olivine and orthopyroxene are more Fe-rich (Fig. 6a and b). AT24 falls between these two groups. A petrological link between Atud gabbronorites and diorites is found in the

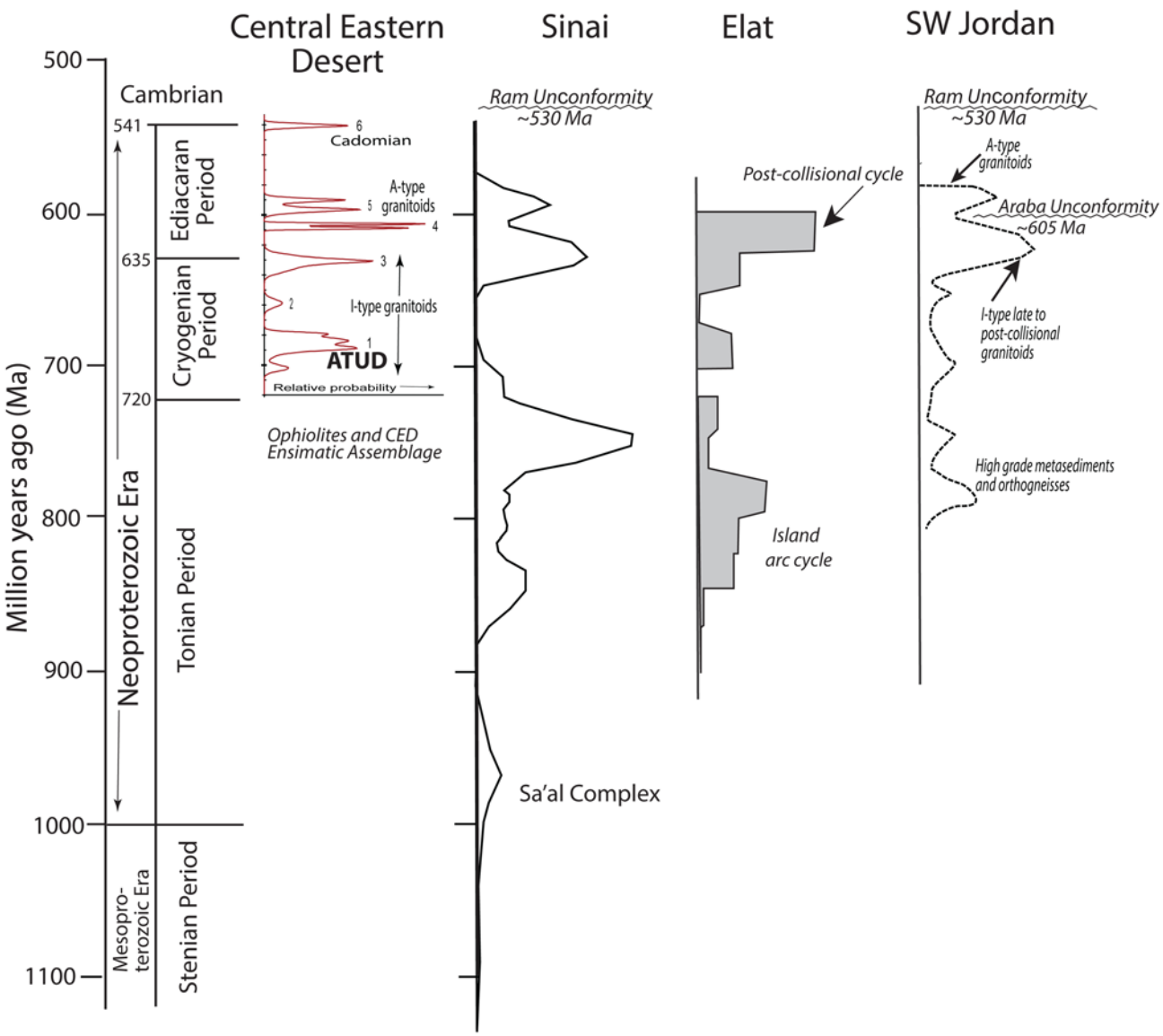

Fig. 3. Magmatic episodes for Central Eastern Desert and Sinai, Egypt and Elat area, Israel, after Stern and Ali (2020). Curve for Jordan is from Jarrar *et al.* (2013), Yaseen *et al.* (2013) and Powell *et al.* (2015). How the Atud igneous complex fits in the temporal evolution of magmatic activity of this region is also shown.

composition of relict CPX and $An_{80–90}$ PL (Fig. 6a, c and d). Based on these compositions, diorites can be divided into two sub-groups. The first group consists of diorites with CPX and calcic PL relics. The core of plagioclase is altered to epidote and albitic plagioclase ($An_{20–30}$). The rim plagioclase is $An_{50–60}$. CPX relics are compositionally identical to those in gabbro (Fig. 6a, c and d). The second group includes quartz diorites, which do not contain relict CPX and PL. The plagioclase in this group is more Na-rich. Plagioclase cores are $An_{50–60}$, which is partly altered to epidote and $An_{10–20}$ PL. Rim PL is $An_{10–30}$ (Fig. 6a, c and d).

Amphibole is found in both gabbro and diorite and formed during magmatism (Si <7.5) and during alteration (Si >7.5). Amphiboles range in composition from actinolite to hornblende to tschermakite (Fig. 6e), but vary in Mg# according to lithology (gabbronorite has higher Mg# than diorite). Magnesio-hornblendes in gabbros exist interstitially or form along the fractures within cpx. High-Si amphiboles (actinolites) mainly exist in fractures and are probably products of hydrothermal alteration. Actinolite group amphiboles (Si >7.5) in diorites are cores with sieve texture (Fig. 5f, the bottom left large grain). Sieve-textured amphibole cores contain plagioclase, quartz and Fe-oxide. These actinolite cores reflect hydrothermal alteration of pyroxenes. Magnesio-hornblende (Si <7.5) in diorite formed later in magmatic evolution. The Mg# of amphiboles in diorite is expected from magmatic equilibrium with whole-rock compositions. Fe-rich amphibole (Mg/(Mg + Fe) 0.4–0.5) formed in rocks with high Fe/Mg ratios (AT4 and 9, Mg# 23–24); the low-Fe amphiboles (Mg/(Mg + Fe) 0.7–0.8) exist in diorites with high Mg (Mg# >49). Aluminium contents in amphiboles vary with lithology and origin: magnesio-hornblende in gabbro contains high aluminium (Al_2O_3 10–12 wt%), whereas diorite has lower aluminium contents (7–9 wt%), and the Al_2O_3 content in actinolite for both gabbro and diorite is 0.5–5 wt% with large variation. In both gabbro and diorite, amphibole rims are variably altered to chlorite.

Mineral equilibration temperatures were determined for gabbroic rocks with different mineral geothermometers (Brey and Köhler 1990; Andersen *et al.* 1993; Putirka 2008) using the average composition of mineral rims determined by EPMA (Fig. 7). The Brey and Köhler (1990) geothermometer focuses on pyroxenes and provides three independent estimates, TBKN by using Fe–Mg–Ca–Na balances in two pyroxenes, TCa-in-opx by using Ca content of orthopyroxene, and TNa by using the partitioning of Na between orthopyroxene and clinopyroxene (Fig. 7). TBKN for Atud gabbros varies from 799 to 913°C. TCa-

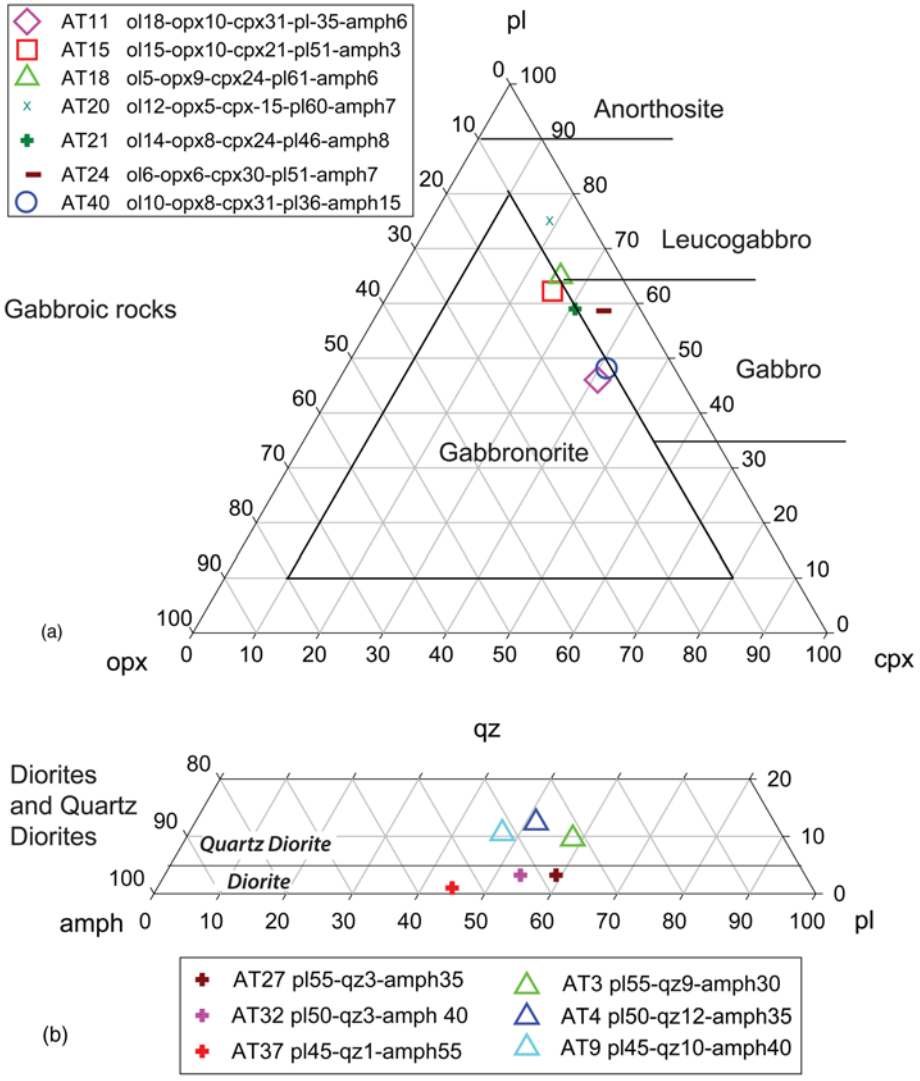

Fig. 4. Modal composition of Atud samples. (**a**) Modal composition of gabbroic rocks; it should be noted that abundance of olivine and hornblende are not shown. (**b**) Modal composition of diorites (<5% quartz) and quartz diorites (>5% quartz). Diagrams are from Streckeisen (1976).

in-opx is in the range of 1022–1067°C and TNa ranges from 859 to 1063°C; one sample gives 859°C, other samples give 1008–1063°C. With QUILF (Andersen *et al.* 1993), temperature is calculated based on Fe–Mg–Ca exchange between clinopyroxene, orthopyroxene and olivine. The estimated temperature is in the range of 892–974°C. Based on the two-pyroxene geothermometer (equation (36)) of Putirka (2008), the estimated temperature is in the range of 914–949°C. Based on the results, the Brey and Köhler (1990) two-pyroxene geothermometers are more sensitive to the mineral chemistry. Because of observed hydrothermal alteration, we are concerned that temperatures estimated based only on a single element (Ca in opx) or in two coexisting minerals (Na in cpx and opx) are unreliable. *T* estimates based on multiple elements in multiple phases (QUILF and Putirka's *T*) show a similar range, and estimates using give the tightest temperature range. For these reasons, we adopt the range of 892–974°C using determined using QUILF and Putirka (2008) two-pyroxene geothermometers (Fig. 7). Even these are re-equilibration temperatures, reflecting when exchange of these cations effectively stopped, so magmatic temperatures were probably higher.

Whole-rock geochemistry

Ten samples of the Atud gabbro–diorite complex were analysed for whole-rock major and trace element compositions (Supplementary Table 2). Two quartz diorites and three diorites along with four gabbronorites and one leucogabbro were analysed. These 10 samples define a mafic complex, with 46.5–54.3 wt% SiO_2 (mean = 48.7 wt%) and 3.14–11.75 wt% MgO (mean = 8.4 wt%); considering data from Abdelnasser and Kumral (2016) extends the compositional range for the complex to 57.8 wt% SiO_2 (Fig. 8a). From our analyses, the Atud complex classifies as subalkaline and mafic on the total alkalis–silica diagram; it should be noted that the three diorites we analysed plot in the field of gabbro, the two quartz diorites plot as gabbro–diorite, and the five gabbroic rocks plot below the gabbro field (Fig. 8a). The AFM diagram shows that the Atud mafic complex is calc-alkaline (Fig. 8b). The Mg#, defined as 100Mg/(Mg + Fe), is high in Atud mafic complex rocks, ranging from 60.6 to 89.4. Nickel content ranges widely, from 155 to 8 ppm. This mafic complex has experienced significant magmatic fractionation and some of the gabbros and diorites may be cumulates. Major incompatible elements TiO_2 and K_2O are low, 0.22–2.21 wt% and 0.05–0.62 wt%, respectively. The Atud complex igneous rocks define a low-K suite (Fig. 8a).

Trace element compositions reveal that the Atud mafic complex is characterized by slightly light rare earth element (LREE)-enriched patterns, with significant positive Eu anomalies (Eu/Eu* = 1.06–1.56, where $Eu/Eu^* = Eu_{ch}/(Sm_{ch} \times Gd_{ch})^{0.5}$; Fig. 8c), discussed further below. These melts do not show strong control by garnet but it is possible that minor residual or fractionating garnet was involved in magma evolution. Extended trace element diagrams are also parallel, with diorites being modestly enriched relative to gabbros and gabbronorite but the quartz diorites being significantly more enriched. Extended trace element patterns are arc-like, with significant

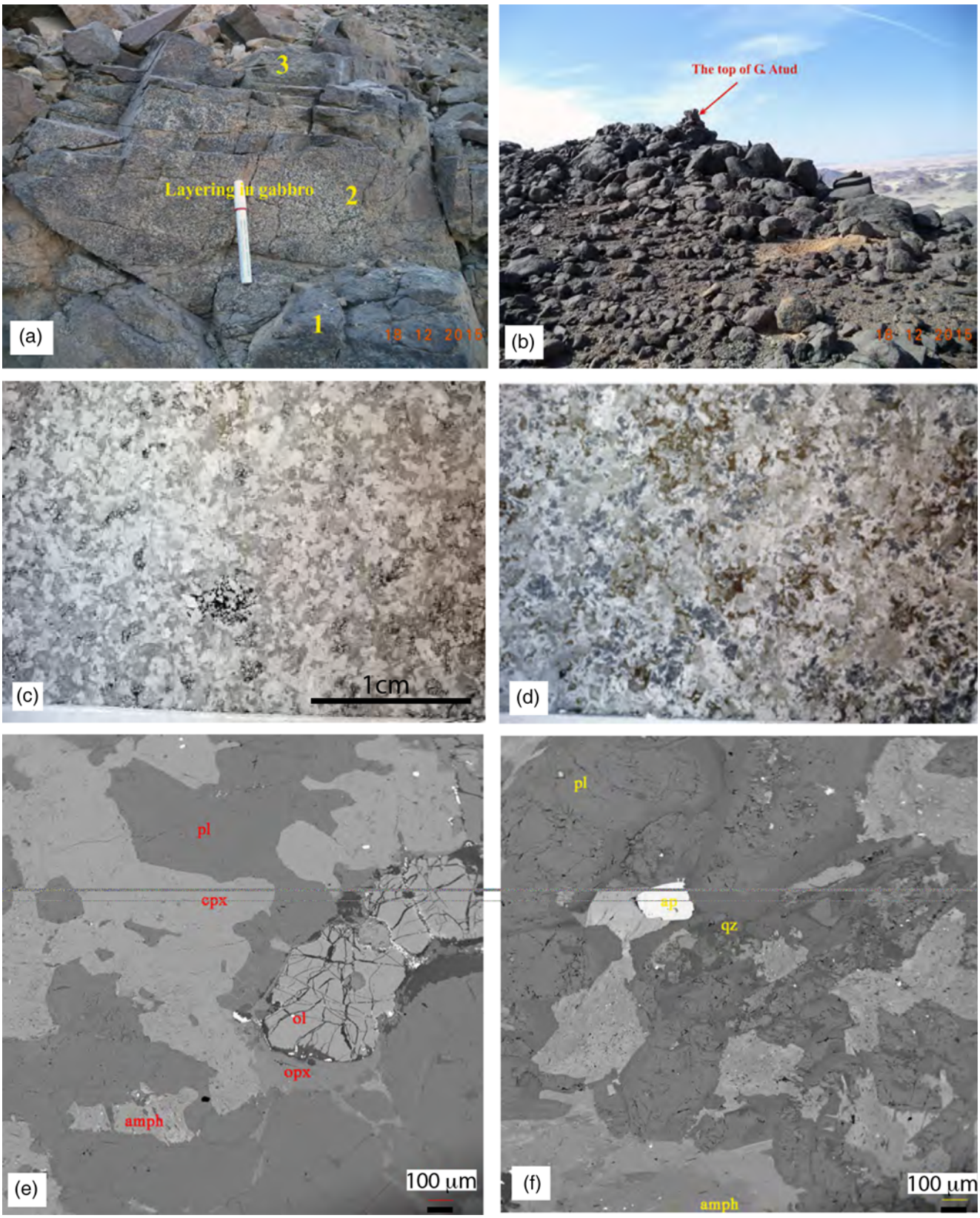

Fig. 5. Field photographs of outcrops of Atud intrusion: (**a**) layering in gabbroic rocks defined by plagioclase-rich band sandwiched between plagioclase-poor layers; photograph by M. Azer; Marker pen is about 15 cm long. (**b**) typical desert weathering of Atud gabbroic rocks; photograph by M. Azer. Large boulders are about 1m across. (**c**) Full thin section photograph of gabbro AT24. (**d**) Full thin section photograph of diorite AT32. (**e**) Back-scattered electron image of Atud AT24 gabbro. (Note olivine ($Fo_{80–81}$), opx, cpx, plagioclase ($An_{80–90}$) and amphibole.) (**f**) Back-scattered electron image of Atud AT32 diorite with zoned amphibole and plagioclase. Each plagioclase grain has a large core ($An_{75–85}$) and a thin rim ($An_{55–61}$). Some plagioclase cores have been altered to epidote with albite-rich plagioclase ($An_{20–25}$).

enrichments in fluid-mobile elements and depletions in Nb and Ta, suggesting formation at a convergent plate margin, in a juvenile arc-like setting. The La/Nb value ranges from 2.2 to 4.8, significantly higher than La/Nb = 1.4 separating arc-like (>1.4) from ocean island basalt (OIB)-like (<1.4) mafic rocks (Condie 1999). These igneous rocks have geochemical features that are most like those of primitive

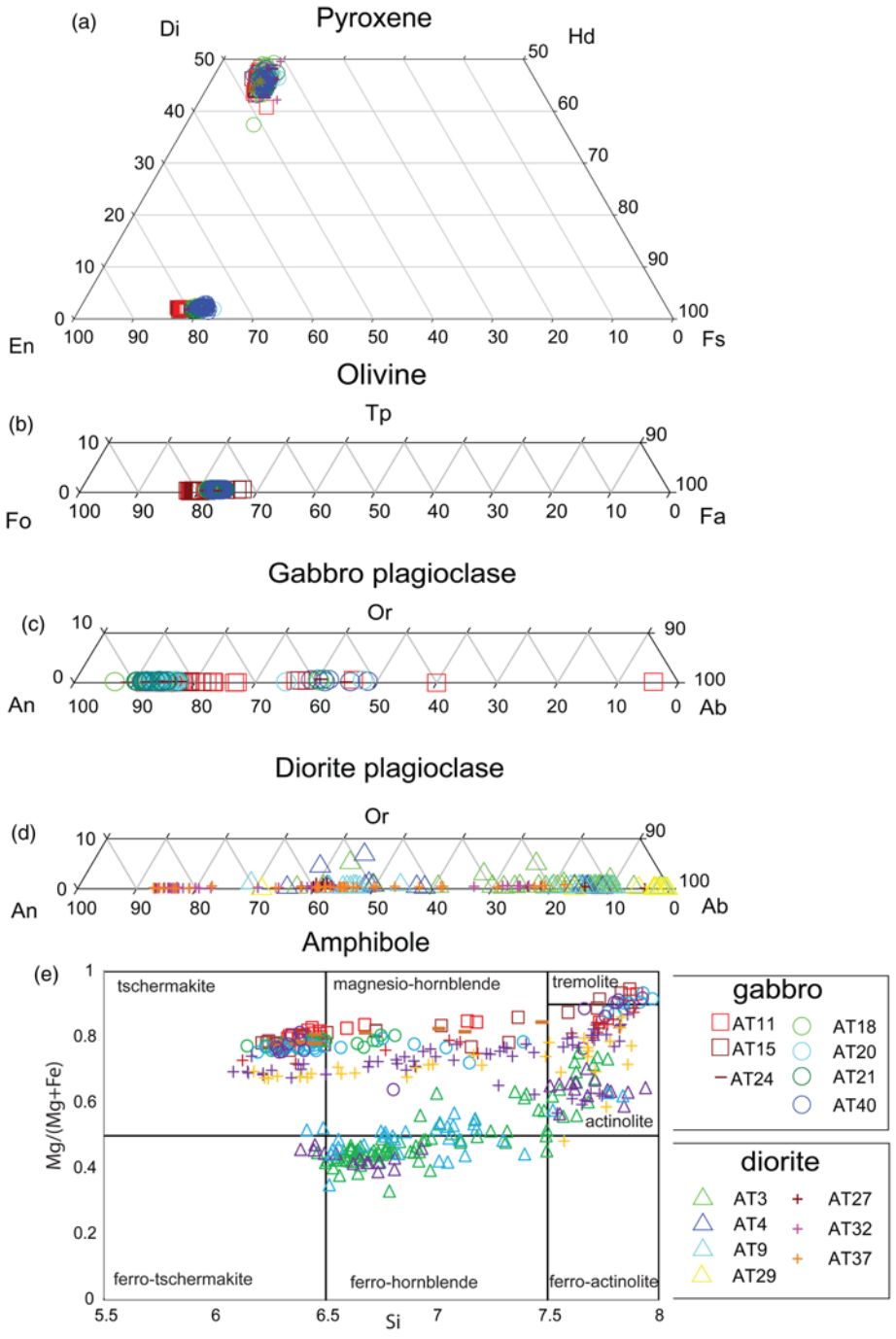

Fig. 6. Compositions of the dominant minerals in the Atud intrusive complex. (**a**)–(**c**) summarize the compositions of pyroxenes (**a**), olivine (**b**) and plagioclase (**c**) in the gabbroic rocks and (**d**) summarizes the composition of plagioclase in the diorites. (**e**) shows the compositions of amphiboles. The restricted range of pyroxene compositions, slightly larger range of olivine compositions, and much wider range of plagioclase compositions for the gabbronorites should be noted. Plagioclase ranges from An_{50} to An_{90} in the gabbronorites, generally more calcic than the mostly $<An_{60}$ composition of diorites, although cores in diorite plagioclase may be as calcic as An_{87}.

arcs. Our gabbro trace element results are more depleted and show a more logical sequence from enrichment gabbro to diorite than the samples analysed by Abdelnasser and Kumral (2016).

Aluminum contents in our analyses range from 15.65 to 26.0 wt% Al_2O_3; analyses of Abdelnasser and Kumral (2016) are in many cases significantly lower, 13.79–18.33 wt%. Such high Al_2O_3 contents are atypical for magmatic rocks and suggest plagioclase accumulation, as might be expected if the Atud mafic complex included some plagioclase-rich cumulates, as suggested here from the REE plots (Fig. 8c). To test this possibility, we examined the behaviour of elements that prefer plagioclase: Sr, Eu, and Al (Fig. 9). Our data show strong covariations between Eu/Eu* v. Sr/Y and Eu/Eu* v. Al_2O_3, indicating an important role for plagioclase accumulation in the magmatic evolution of the Atud complex. In contrast, the data of Abdelnasser and Kumral (2016) show no such covariation, in spite of the fact that their data include a sample with Eu/Eu* as high as 1.8, significantly higher than our maximum value of *c.* 1.6. It is worth noting that adakite-like Sr/Y values as high as 90 are found for a couple of our analyses, but this reflects plagioclase accumulation. Sr/Y is <30 for all Abdelnasser and Kumral (2016) analyses. Assuming the parental magma of the Atud complex had Eu/Eu* *c.* 1.0, we infer this had Sr/Y *c.* 20 and *c.* 15 wt% Al_2O_3, similar to mid-ocean ridge basalt (MORB). Sr/Nd values are also high (31–173), reflecting combined effects of high Sr/Nd in arc magmas plus effects of plagioclase accumulation. The Th/U values range from 2 to 3.2, reflecting subduction-related U enrichment.

U–Pb zircon geochronology

Two quartz diorites (AT4, AT9) and one gabbronorite (AT40) were selected for U–Pb zircon age determinations; sample locations are shown in Figure 2. Analytical results are given in Supplementary Table 3 and shown in Figure 10.

Sample AT4 is a coarse-grained quartz diorite. Zircons separated from it are euhedral (100–200 μm) and yellow to pale brown. Uranium and thorium contents are generally low, with a median of

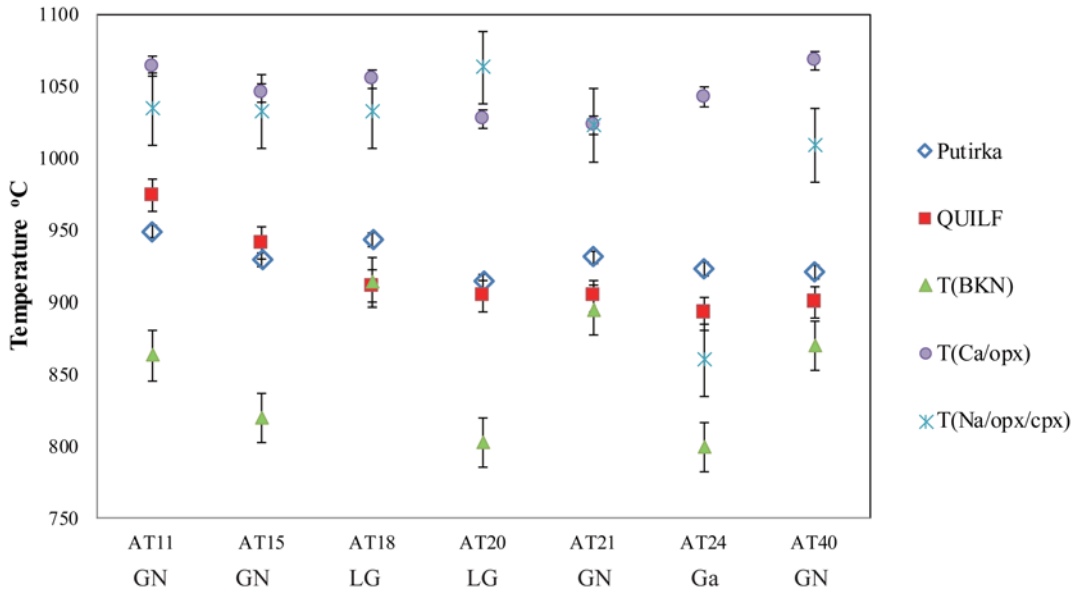

Fig. 7. Summary of calculated mineral equilibrium temperatures for Atud mafic igneous rocks (GN, gabbronorite; LG, leucogabbro; Ga, gabbro). Mineral equilibration temperatures were determined with different geothermometers (Brey and Köhler 1990; Andersen *et al.* 1993; Putirka 2008). Putirka, two-pyroxene method of Putirka (2008); QUILF, Fe–Mg–Ca exchange between clinopyroxene, orthopyroxene and olivine (Andersen *et al.* 1993); T(BKN), Brey and Köhler (1990) two pyroxene using Fe–Mg–Ca–Na between two pyroxenes, T(Ca/opx), using Ca content of opx (Brey and Köhler 1990); T(Na/opx/cpx), using the partitioning of Na between Opx and Cpx (Brey and Köhler 1990).

295 ppm and 180 ppm respectively, but in one case range up to almost 5000 ppm and 7000 ppm respectively. Th/U ratios are typically magmatic, in the range 0.4–1.5. Twenty-eight measurements were made on 22 grains. All analyses are concordant (Fig. 10a), but three spots (zr-2, zr-13 and zr-22) have a high analytical uncertainty resulting from correction for high common Pb content and have been omitted from further discussion. The remaining 25 analyses cluster tightly, defining a concordia age of 691.4 ± 2.8 Ma (2σ; MSWD = 0.8; Fig. 10a).

Sample AT9 is a coarse-grained quartz diorite. Zircon recovered from this sample is subhedral to euhedral and yellow to pale brown. A total of 21 measurements were made on 18 zircons. Uranium and thorium contents are very similar to sample AT4, with median concentrations of 300 ppm and 200 ppm respectively. Th/U is in the range 0.35–1.2, again typically magmatic. All analyses are concordant but three spots (zr-1, zr-18 and zr-24) have a high analytical uncertainty and have been omitted from age calculation. The remaining 18 analyses yield a concordia age of 698.3 ± 3.1 Ma (Fig. 10b) based on a group of concordant analyses (MSWD = 0.85; Supplementary Table 3). Given the likelihood that both diorite samples have a common age, combining their U–Pb data (43 accepted analyses) yields a concordia age of 694.5 ± 2.1 Ma (MSWD = 0.95; Fig. 10c). We interpret this as the age of intrusion and crystallization of the Atud quartz diorites.

Sample AT40 is a coarse-grained greenish gabbronorite. Zircon recovered from the gabbro is euhedral (100–200 μm) and yellow to pale brown. Uranium and thorium concentratios have median values of 540 ppm and 350 ppm respectively, although several grains exceed 2000 ppm for both elements, in one case up to 5600 ppm for U and 8300 ppm for Th. Th/U ratios range from 0.46 to 1.47. Twenty-six measurements were made on 21 grains. Six spots are removed from age calculation because they have high analytical uncertainty resulting from correction for high common Pb content and have been omitted from further discussion. The remaining 20 concordant analyses cluster tightly, defining a concordia age of 695.3 ± 3.4 Ma (95% confidence level, MSWD = 1.2; Fig. 10d). In summary, the magmatic ages obtained for zircon from the above three samples are identical within uncertainty, which we interpret to record the age of crystallization of the Atud intrusion at *c.* 695 Ma.

Sr–Nd–Pb–O isotopes

Zircons from the three dated samples (AT4, 9 and 40) were analysed for O isotopes (Supplementary Table 4; Fig. 11a). Zircons from quartz diorites AT4 and AT9 are indistinguishable from those of gabbronorite AT40, with $\delta^{18}O$ varying from +3.5 to +7‰, straddling the value of 5.3 ± 0.6‰ for zircon from mantle-derived melts (Fig. 11a).

Ten whole-rock samples were analysed for Sr, Nd and Pb isotopic compositions (Supplementary Table 5). Initial $^{87}Sr/^{86}Sr$ values calculated for 690 Ma are low, ranging from 0.70246 to 0.70268. This tight range shows little evidence of open-system alteration. Epsilon-Nd calculated for 690 Ma (εNd_{690}) ranges from +4.2 to +7.3, with broadly overlapping ranges for gabbroic and dioritic rocks, although the dioritic rocks have mostly higher εNd_{690} (Fig. 11b). The Sr and Nd isotopic results indicate that Atud diorites and gabbronorites were derived from a depleted mantle source; contributions from juvenile lower crust are also possible. Pb isotopic results are also broadly similar, with $(^{206}Pb/^{204}Pb)_{690} = 17.1–18.8$, $(^{207}Pb/^{204}Pb)_{690} = 15.46–15.65$ and $(^{208}Pb/^{204}Pb)_{690} = 36.9–38.6$ (Fig. 11c and d). In detail, two gabbroic samples contain significantly more radiogenic Pb than do the diorites and the other gabbros.

Discussion

Our new results for the Atud igneous complex provide important new constraints for understanding how it formed and therefore on the construction of new continental crust at the end of the Precambrian. Four important constraints are outlined below.

Age of the Atud igneous complex

The first important constraint is that the Atud gabbro and its envelope of diorite and quartz diorite were emplaced together *c.* 690 myr ago. This igneous complex is composed of low- to medium-K calc-alkaline igneous rocks that formed early in the Cryogenian evolution of the Eastern Desert of Egypt (Fig. 3).

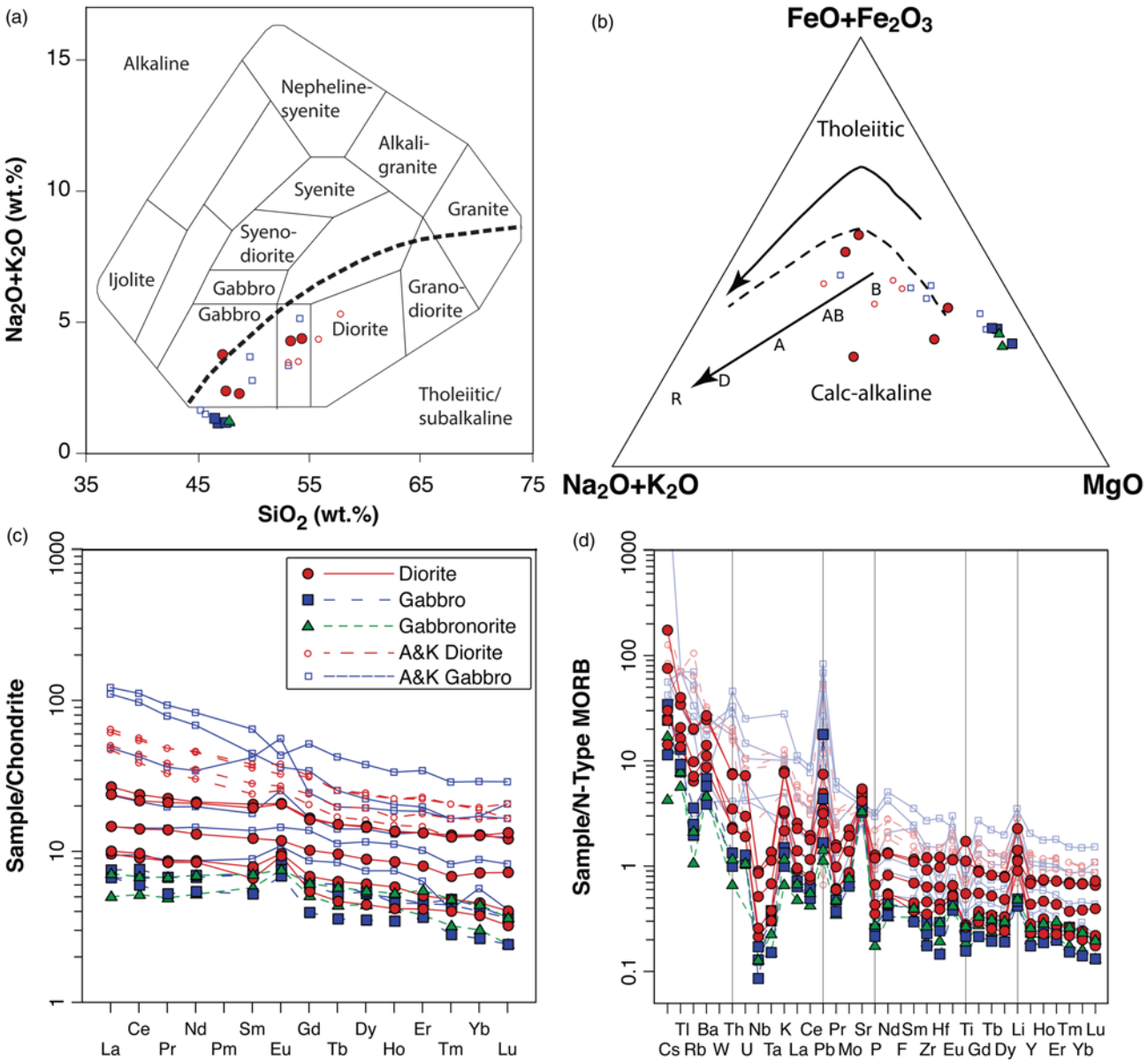

Fig. 8. Whole-rock chemical composition of Atud complex igneous rocks. (**a**) Total alkalis–silica diagram showing the subalkaline mafic nature of Atud complex rocks. Data from Abdelnasser and Kumral (2016) are also shown for comparison. Figure is from Wilson (1989) . (**b**) AFM diagram revealing calc-alkaline nature of Atud igneous rocks. B, basalt; AB, basaltic andesite; A, andesite; D, dacite; R, rhyolite. Dashed line separates tholeiitic and calcalkaline fields (Irvine and Baragar 1971). (**c**) Chondrite-normalized REE diagrams for Atud igneous rocks. Data from Abdelnasser and Kumral (2016) (A&K) are also shown for comparison. (**d**) Normal mid-ocean ridge basalt (N-MORB) extended trace element diagrams for Atud igneous complex rocks. Data from Abdelnasser and Kumral (2016) (A&K) are also shown for comparison. Strong enrichments in large ion lithophile elements, K, Pb, Sr and Li, and strong depletions in Nb and Ta should be noted.

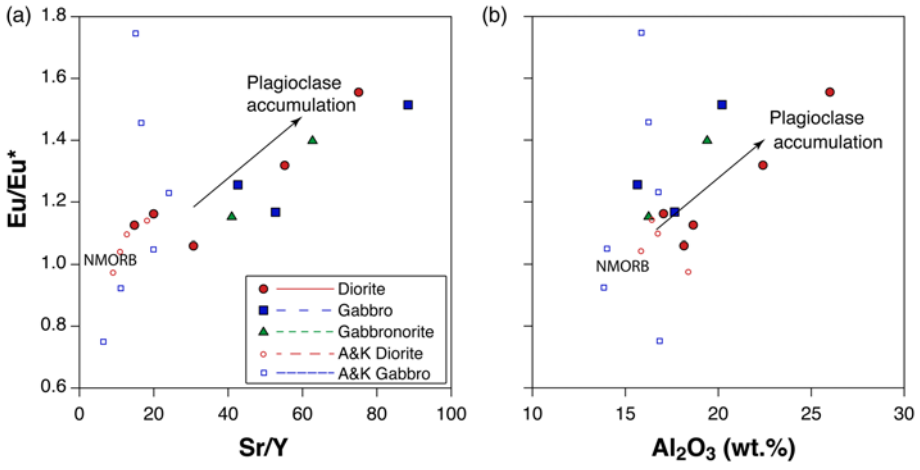

Fig. 9. Trace element evidence for plagioclase control in Atud complex magmatic evolution. (**a**) Eu/Eu* v. Sr/Y. High Sr/Y and Eu/Eu* indicates significant plagioclase accumulation. (**b**) Al_2O_3 v. Eu/Eu*. High Al_2O_3 v. Eu/Eu* indicates significant plagioclase accumulation.

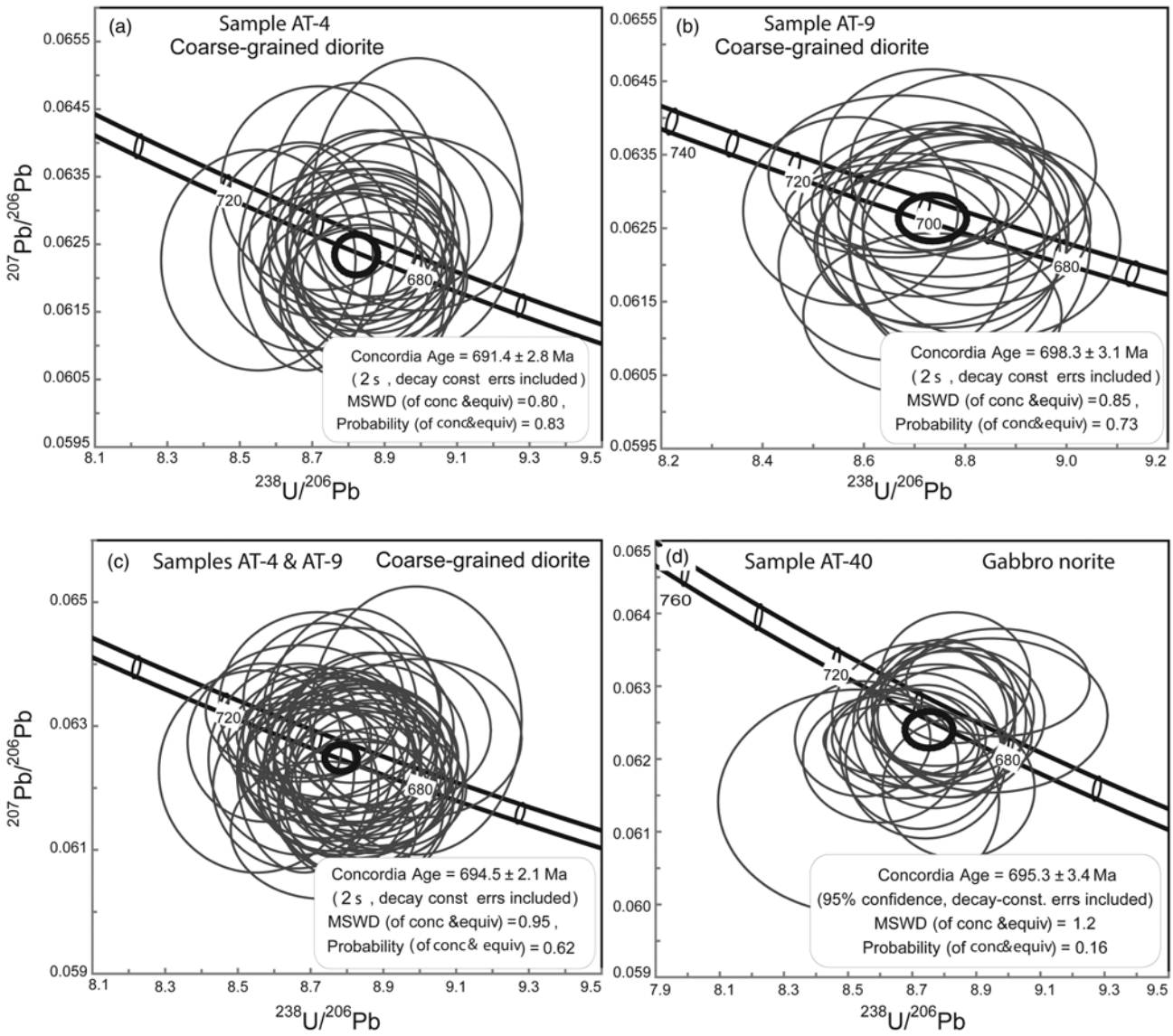

Fig. 10. Concordia diagrams after Tera and Wasserburg (1972): (**a**, **b**) U–Pb zircon ages for two samples of diorite (**a**, AT4; **b**, AT9); (**c**) combined age of diorite samples; (**d**) age of gabbronorite AT40.

Source of Atud complex parental magmas

The second important result of our study is that Atud complex magmas mostly represent juvenile contributions from the mantle, although contributions from juvenile lower crust are also possible. Atud magmas may have been primitive (gabbro) or evolved (diorite–quartz diorite) but in either case their primarily juvenile nature is demonstrated by Nd, Sr and zircon O isotopic compositions. Epsilon-Nd calculated for 690 Ma (εNd_{690}) ranges from +4.2 to +7.3 with a mean εNd_{690} of +5.6 and modest variation between gabbroic and dioritic rocks (Fig. 11b). Depleted mantle of *c*. 700 Ma is estimated to have $\varepsilon Nd_{690} = +6.6$ according to the model of DePaolo (1981) and $\varepsilon Nd_{690} = +8.6$ according to the model of Goldstein *et al.* (1984), so Atud complex igneous rocks have εNd_{690} that plots to the right of the mantle array, very close to the isotopic composition expected for depleted mantle at that time. The average initial $^{87}Sr/^{86}Sr$ value at 690 Ma is 0.70260, also similar to or even less radiogenic than depleted mantle at that time (Fig. 11b). In spite of these observations, it is possible that Atud magmas assimilated some slightly older crust and/or sediments. The three samples with the lowest εNd_{690} may have been most affected by crustal material, although these are gabbroic. Because of the relatively high contents of Sr and Nd, a small addition of crust may result in no or only small shifts in the Sr and Nd isotopic composition. In contrast, because of the small amount of Pb in the mantle, the Pb isotopic composition of mantle-derived magmas is affected more significantly by adding small amounts of granitic crust and/or sediments.

In the absence of compelling isotopic evidence demanding crustal sources or substantial crustal residence time, the controversy over mantle versus crustal sources for the parent magma depends on physical arguments. On the one hand, direct mantle derivation of the mafic parental magma (with fractionation and limited assimilation in the lower crust before the residual liquid ascends to the depth of emplacement) is a simple and physically straightforward model. By contrast, the suggestion that all mantle-derived mafic material lost enough heat to freeze completely and form solid lower crust and was then reactivated by heating nearly to its liquidus (without the passage of sufficient time to evolve isotopically) seems complex and challenging to realize from a heat-budget point of view. Whereas there are numerous thermal models of the derivation of felsic magma by crustal melting (e.g. Laube and Springer 1998; Annen *et al.* 2006; Bea 2012), we are not aware of any serious suggestions that mafic magma can be dominantly sourced from high-degree melting of mafic crust.

Zircon O isotopes are useful for recognizing whether a magma was generated by melting of sediments or altered rocks or interacted

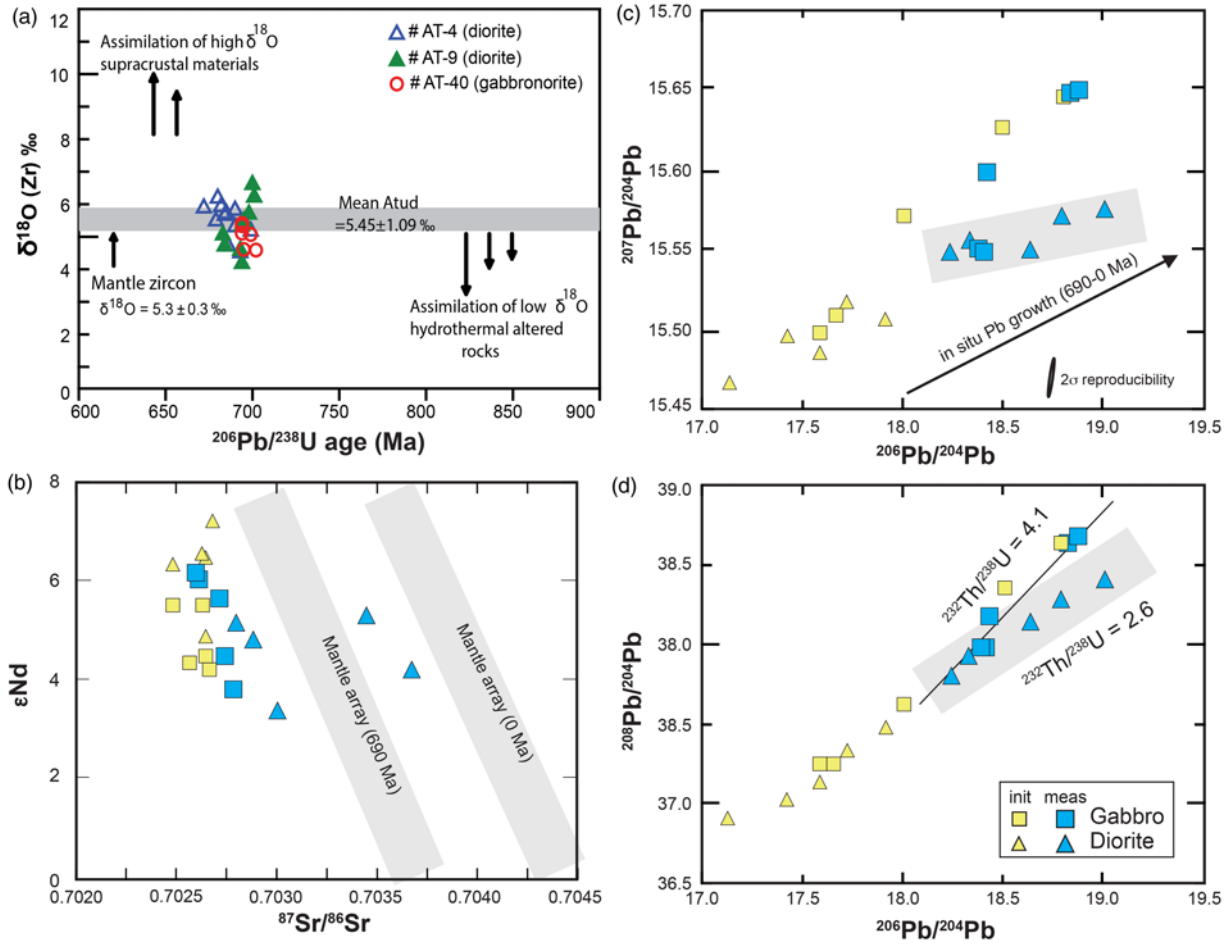

Fig. 11. Isotopic results. (**a**) Single zircon $\delta^{18}O$ data for samples with $^{206}Pb/^{238}U$ ages, filtered to remove data on cracks, etc. Field of mantle zircon from Valley *et al.* (1998). (**b**–**d**) Measured (blue) and initial (yellow) isotopic compositions of Sr, Nd and Pb for Atud gabbro and diorite samples; corrections for radiogenic growth use trace element abundances from Supplementary Table 2. Initial isotopic data fall on binary mixing lines in all diagrams. In (**b**), the data fall to the left of the mantle array for 690 Ma, largely owing to low initial $^{87}Sr/^{86}Sr$, which is also known from xenoliths from the Arabian and East African lithospheric mantle (e.g. Meshesha *et al* 2011; Bianchini *et al.* 2014). The scatter in the measured Pb isotopic composition is the result of post-emplacement *in situ* radiogenic growth (blue symbols) that is more important in the dioritic samples than in the gabbroic samples. It should be noted that diorites and gabbros have different post-emplacement $^{232}Th/^{238}U$ values.

significantly with such materials (Valley 2003; Zheng *et al.* 2004, 2006; Be'eri-Shlevin *et al.* 2009, 2010). The mean $\delta^{18}O$ zircon value of +5.45‰ for Atud complex rocks overlaps that of 5.3 ± 0.6‰ for mantle zircon (Valley 2003), consistent with the juvenile nature of Atud complex magmas (Fig. 11a), although there are indications of minor alteration. Zircons from the Atud complex with $\delta^{18}O$ lower than mantle values of ~ +5.3 ± 0.6‰ (Valley *et al.*, 1998) can be explained by the incorporation of small admixtures of rocks that were hydrothermally altered by meteoric water at high temperature (>300°C), such as lower oceanic crust (Wei *et al.* 2002; van Schijndel 2013) or crystallized from an isotopically heterogeneous low-$\delta^{18}O$ magma formed from protoliths previously altered by meteoric fluids (Liu and Zhang 2013).

There is no evidence for pre-existing older crust in the 41 zircons that we analysed. There is isotopic evidence for two-component mixing. One component is depleted mantle. The other component may be metasomatized mantle or lower crust. The depleted component is more prominent in the diorites. In the $^{207}Pb/^{204}Pb$ v. $^{206}Pb/^{204}Pb$ diagram (Fig. 11c), the diorites plot at the lower end of the trend, but overlap with the gabbro samples. The difference between gabbros and diorites cannot be explained by *in situ* growth of radiogenic Pb (arrow), but must instead reflect initial heterogeneity. The higher $^{207}Pb/^{204}Pb$ of the gabbros implies a higher crustal Pb component. The most radiogenic gabbro Pb is close to the composition of the metasomatic component (mass balance; much higher Pb in the crust or metasomatic component than in the depleted mantle). The gabbro samples have less *in situ* growth and, therefore, plot closer to the initial mixing line. In contrast, the diorites had greater *in situ* growth. In the $^{208}Pb/^{204}Pb$ v. $^{206}Pb/^{204}Pb$ diagram (Fig. 11d), the diorites define a Th/U value of about 2.6, which is typical for variably evolved crustal magmatic rocks, and similar to the mean Th/U of 2.79 ± 0.36 measured for the rocks (Supplementary Table 2). The depleted mantle endmember has εNd_{690} ~+8 or higher and initial $^{87}Sr/^{86}Sr$ slightly less than 0.7025. This endmember has $^{206}Pb/^{204}Pb$ *c.* 17.1, $^{207}Pb/^{204}Pb$ *c.* 15.47 and $^{208}Pb/^{204}Pb$ *c.* 36.8. The metasomatized mantle endmember has εNd_{690} ~+4 or less, $^{87}Sr/^{86}Sr$ around 0.7027 or slightly higher, $^{206}Pb/^{204}Pb$ *c.* 19.0, $^{207}Pb/^{204}Pb$ *c.* 15.65 and $^{208}Pb/^{204}Pb$ *c.* 38.8. It should be noted that the sample with the most radiogenic Pb isotopic composition had hardly any correction for *in situ* Pb growth. The high $^{207}Pb/^{204}Pb$ provides strong evidence for the participation of old crustal Pb, perhaps derived from subducted sediments.

Tectonic setting where Atud igneous complex formed

The third important constraint from our study is that the Atud igneous complex formed in association with a convergent plate margin. This is reflected in the hydrous nature of the melts as shown by the abundance of amphibole along with the observed trace element patterns and ratios characteristic of intra-oceanic arc

magmas (Fig. 8d). The large range in initial Pb isotopic compositions observed for Atud igneous rocks is also consistent with formation over a subduction zone. There is evidence that *c*. 690 Ma igneous activity was widespread in the region around the Atud complex, as would be expected for a convergent margin. The Hafafit dome to the south (Fig. 1b) provides evidence for about 23 myr of igneous activity around the time of Atud magmatism: U–Pb zircon age of 682 Ma for a tonalite (Stern and Hedge 1985) and three gneiss samples with $^{207}Pb/^{206}Pb$ single zircon evaporation ages between 677 ± 9 and 700 ± 12 Ma (Kröner *et al.* 1994). Stern and Hedge (1985) also reported that the Hafafit tonalite had initial $^{87}Sr/^{86}Sr = 0.7024$, similar to the Atud igneous complex. Cryogenian granitic gneisses are also documented to the north in the El-Sibai complex (679–685 Ma; Augland *et al.* 2012) and to the NW at Wadi Mia (Rb–Sr whole-rock isochron age of 674 ± 13 Ma, $^{87}Sr/^{86}Sr_i = 0.7024$; Stern and Hedge 1985) (Fig. 1b). Hafafit tonalitic gneisses dated by Kröner *et al.* (1994) contain 65–75 wt% SiO_2 and have low K_2O contents (0.78–0.84 wt%), consistent with derivation from parental magmas like those of the MED complex, which is also characterized by low K_2O contents. Kröner *et al.* (1994) also reported analyses of interlayered gabbroic rocks in the Hafafit dome; these are characterized by low TiO_2 and K_2O contents (0.44–0.88 wt% and 0.18–0.33 wt%, respectively) and moderately high MgO contents (6.6–7.7 wt%), similar to the compositions of Atud gabbroic rocks. Some of these mafic interlayers may be related to the magmatic episode responsible for Atud gabbroic rocks.

We do not know the geometry of the *c*. 690 Ma convergent margin. The geological map of the region (Fig. 1b) shows that the MED complex defines an east–west-trending belt centred on 25°15'N, suggesting that the convergent margin trended east–west (present coordinates). The presence of similar-age gneisses in the Hafafit dome to the south, and to the NE in the El-Sibai complex and at Wadi Mia, invites speculation that these more felsic bodies formed above the MED. If so, the east–west-trending MED region in the Central Eastern Desert represents a broad antiform.

Petrological evolution of the Atud igneous complex

Our fourth constraint is that dioritic and gabbroic rocks of the Atud igneous complex are complementary representatives of a heterogeneous mafic–intermediate complex. A petrological link between Atud gabbros and diorites is found in the composition of relict CPX and $An_{80–90}$ Pl cores in the diorites, as well as geochemical and isotopic similarities. We do not know the dimensions of the larger complex represented by outcrops around Gebel Atud but it is reasonable to infer that it extends significant distances in all directions. Attention has been focused on outcrops around Gebel Atud because of its fresh, distinctive gabbro and diorite-associated gold mineralization. However, it is likely that much of the results for Atud (composition, age and magma source) also applies to other parts of the MED complex in the vicinity. Our results thus provide important insights on the MED complex in the Central Eastern Desert.

We want to know what was the emplacement depth of the Atud igneous complex. The contact between gabbronorite and diorite is diffuse, suggesting emplacement at some depth in the crust. Slow cooling to create coarse-grained plutonic rocks is also consistent with emplacement at some depth in the crust. Amphibole compositions can be used to evaluate the pressure where Atud magma crystallized. We use the Mutch *et al.* (2016) equation for calculating pressure. Using the amphibole Al barometer in the Atud diorites requires extra attention because the amphiboles show altered actinolite cores mantled by magmatic magnesio-hornblende. These core–rim features are especially common in quartz diorite (AT3, 4, 9). For these, the average Al-in-Hb pressures are in the range of 2.9–3.4 kbar. For Atud diorites, amphiboles can be separated into low-Al and high-Al groups, The low-Al group yields 2.7–3.0 kbar, whereas the high-Al group yields 5.1–5.3 kbar. Actinolite cores give 0.86–1.16 kbar. The core–rim amphibole pairs in diorite might not represent the equilibrium condition. The high-Al amphiboles in diorite might be the relicts of amphibole, which was in equilibrium with melt. For gabbro, amphiboles exist interstitially or following fractures within the cpx; we interpret these as forming during a late, volatile-rich stage when it replaced cpx. Magnesio-hornblendes from different gabbro samples have similar chemistry (Fig. 6e); the pressure based on Al content gives 4.5–5 kbar. The actinolites in the fractures give 0.53–1.08 kbar, with one sample giving 2.21 kbar. The estimated intrusive depth is around 13–15 km. The altered amphiboles (actinolite) cannot be used to make pressure estimates.

Petrological modelling

Olivine compositions constrain the composition of the Atud mafic parental magma. AT11 contains the most magnesian olivine, Fo_{81}. These olivines are in equilibrium with a melt with Mg# *c*. 62 (assuming a $K_{D(ol–liq)(Fe–Mg)} = 0.32$ (Roeder and Emslie 1970)). These calculated melt Mg# values are too low to be in equilibrium with unfractionated mantle-derived melts, although if there was a significant proportion of ferric iron in the magma (arc magma Fe^{3+}/total Fe = 0.25) then Atud gabbros may represent unfractionated additions from the mantle.

The Atud gabbronorite body may be fresh because it was one of the last mantle additions to the MED complex MASH zone and was therefore subjected to less mixing and alteration than other parts of the MED complex. If this interpretation is correct, it further suggests that this MASH zone shut down around 690 Ma, consistent with the observed ages of Central Eastern Desert igneous rocks, which are rare between 677 and *c*. 640 Ma (Fig. 3). We have no constraints on when the MED began to form or how long it lasted, although the presence of arc volcanic rocks as old as *c*. 750 Ma in the Central Eastern Desert (Ali *et al.* 2009, 2010) suggests that an arc magmatic system associated with the MED MASH zone lasted for *c*. 60 myr. It is unknown how and when the Atud complex and adjacent MED exposures were uplifted and exposed, but the most likely cause was transpressional deformation associated with Najd deformation *c*. 600 Ma (Hagag *et al.* 2018).

The overall petrological relationship of the Atud sample suite can be modelled by combining fractional crystallization of our most primitive gabbro sample (AT11) with accumulation of An_{60} plagioclase. An illustrative model is shown in Figure 12. Isobaric fractional crystallization was modelled with the rhyoliteMELTS model (Gualda *et al.* 2012) using the alphaMELTS software package (Smith and Asimow 2005), which implements tracking of trace elements alongside the thermodynamic modelling of the major elements. After exploring a range of pressure, oxygen fugacity and initial water contents, we found a reasonable liquid line of descent leading from the most primitive gabbro through most of the gabbronorites to the quartz diorites. The selected fractionation conditions are 0.2 GPa pressure, the nickel–nickel oxide (NNO) fO_2 buffer, and 1.0 wt% H_2O in the AT11 starting liquid. However, the performance of the model is weakly dependent on these parameters; for example, pressures as high as 0.5 GPa work nearly as well, so this choice of model pressure should not be interpreted as a significant constraint on (or preference for) the fractionation or emplacement pressure. The fractionation sequence according to rhyoliteMELTS is olivine (appearing on liquidus at 1320°C), clinopyroxene (appearing at 1210°C and liquid MgO = 10.41 wt%), plagioclase (appearing at 1191°C and 9.45 wt% MgO), magnetite (at 1058°C and 4.02 wt% MgO) and orthopyroxene replacing olivine (at 1017°C and 2.99 wt% MgO). Supplementary Table 7 includes all set-up information and output of the alphaMELTS models. The last olivine to precipitate is Fo_{74}, matching the most

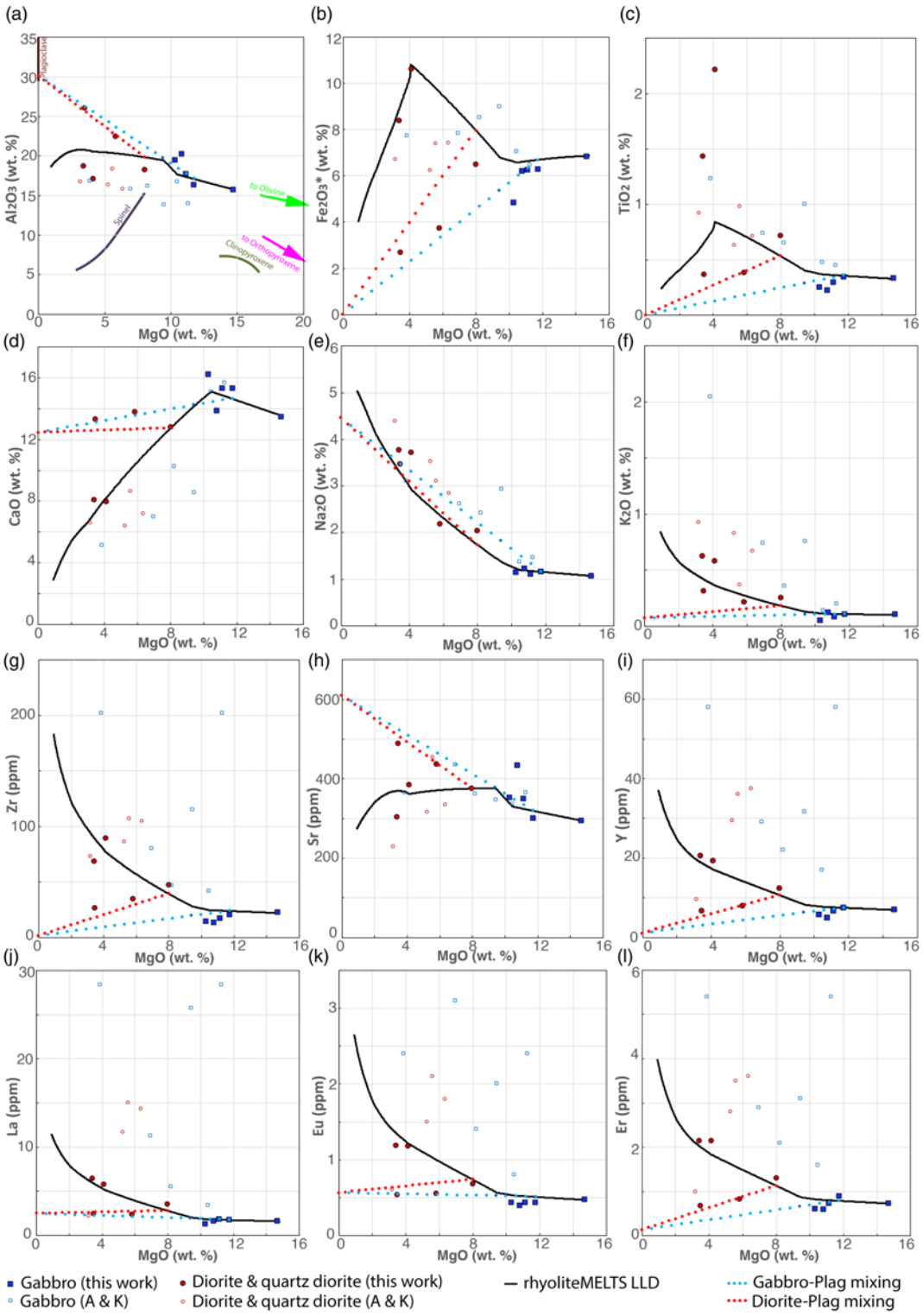

Fig. 12. MgO variation diagrams showing liquid line of descent (continuous black line) and plagioclase admixture (dotted red lines) models for the major and trace element evolution of the Atud mafic suite. Symbols are the same in every panel. The bold black curve shows the liquid line of descent of primitive gabbro AT11 calculated with rhyoliteMELTS at 0.2 GPa, NNO oxygen buffer and 1.0 wt% H_2O in the primary liquid. The dotted lines show mixtures between two selected liquids on this trend with An_{60} plagioclase calculated to be in equilibrium with a more evolved liquid occurring later in the trend. (**a**) Al_2O_3. (**b**) Fe_2O_3*. (**c**) TiO_2. (**d**) CaO. (**e**) Na_2O. (**f**) K_2O. (**g**) Zr. (**h**) Sr. (**i**) Y. (**j**) La. (**k**) Eu. (**l**) Er. Other major and trace elements are shown in Supplementary Table 6.

evolved olivine observed. The model predicts a liquidus olivine of Fo_{93} in AT11, notably more primitive than olivine cores in sample AT11. It is likely either that this high-temperature olivine re-equilibrated to lower Fo content or that AT11 itself includes accumulated olivine and was never a liquid with 14.7 wt% MgO. Model plagioclase ranges from An_{92} down to An_{57}, matching the range seen in the observed mineral chemistry of the suite. As can be seen in Figure 12, this liquid line of descent reasonably fits gabbronorite AT40 (which is related to AT11 by olivine fractionation or accumulation only) in both major and trace elements. However, the other gabbro samples (AT15, AT18 and AT20) show features that deviate from the liquid line of descent:

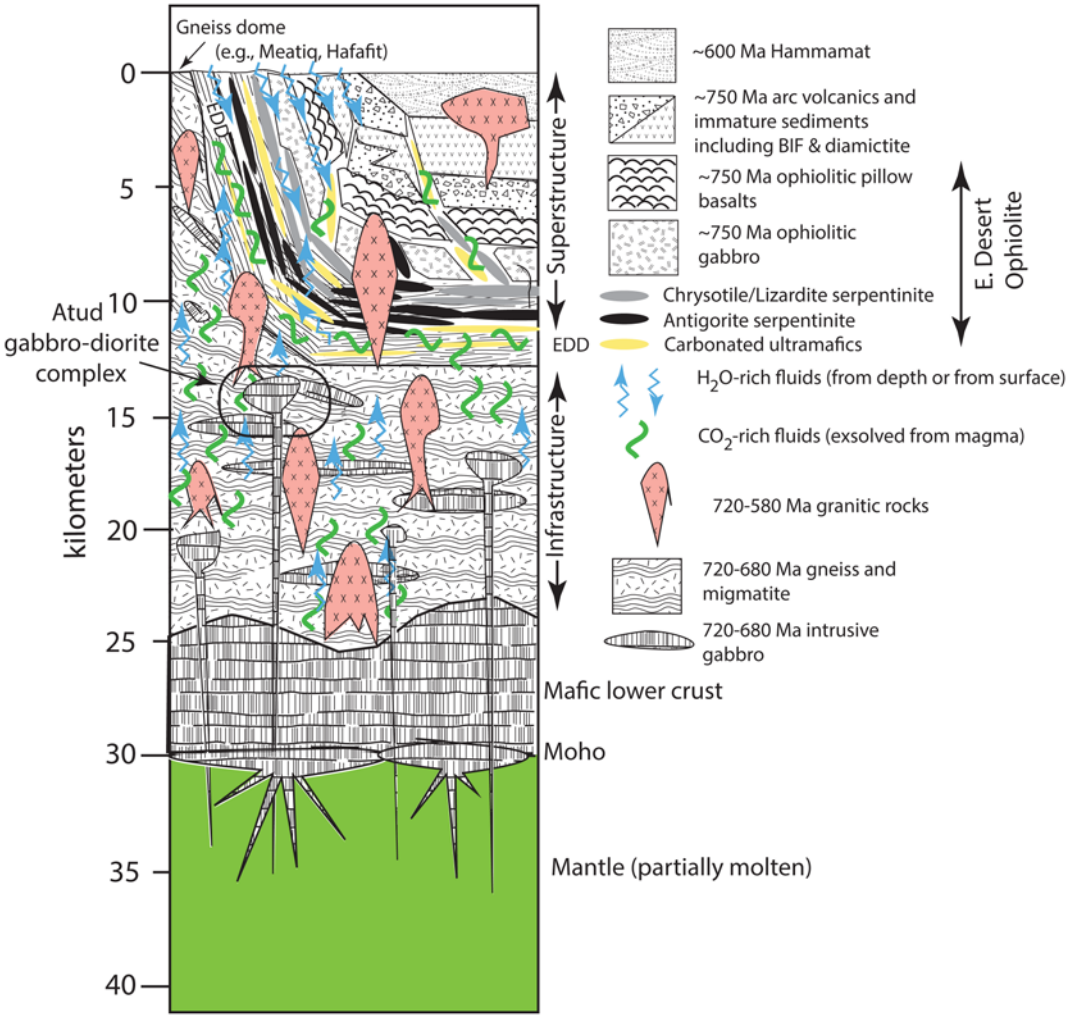

Fig. 13. Schematic diagram illustrating crustal structure and processes beneath the Central Eastern Desert including situation of Atud gabbro–diorite complex in the middle lower crust. Partial melting of depleted upper mantle produces large volumes of volatile-rich, mafic magma; this was mostly underplated to the base of the crust but also was emplaced higher in the infrastructure. These magmas heat amphibolites and gneisses to generate granitic melts. Most of the deformation in the upper plate (superstructure) and along the Eastern Desert Detachment (EDD) happened after emplacement of the Atud gabbro diorite complex, at *c*. 600 Ma).

decreasing TiO_2, sharply decreasing Fe_2O_3* and decreasing concentrations of nearly all incompatible trace elements (Y, Zr and REE except Eu are shown in Fig. 12; others in Supplementary Table 7). The trends through the four more evolved gabbros in many cases can be seen, despite some scatter, to define linear trends in most variation diagrams, pointing in several cases towards the origin.

Turning to the diorites, the liquid line of descent passes very close to the bulk composition of the quartz diorites AT4 and AT9, especially fitting well their distinctive low CaO, low Al_2O_3, high Fe_2O_3*, enrichment in most incompatible trace elements (e.g. Y, Zr and REE are shown in Fig. 12; others in Supplementary Table 7) and lack of Sr enrichment. Compared with the liquid line of descent, they in fact appear over-enriched in some incompatible elements (Ti, K and large ion lithophile elements), which is not unusual in fractionation modelling and may reflect the neglect of amphibole as a fractionating phase (it removes more mass per unit decrease in MgO than does clinopyroxene). It should be noted that the quartz diorites distinctively lack relict minerals and so it is satisfying that they appear to represent quenched liquid compositions along the liquid line of descent. On the other hand, the remaining diorites (AT27, AT29 and AT37), which do contain relict phases suggesting disequilibrium, do not lie on the liquid line of descent. Like the more evolved gabbros, they systematically deviate towards low TiO_2 and Fe_2O_3*, high CaO and Al_2O_3, and decreasing concentrations of incompatible trace elements (Y, Zr and REE including Eu are shown in Fig. 12; others in Supplementary Table 7) except Sr. It is remarkable, more so than in the case of the gabbros, that in almost every MgO variation diagram, the trend through the diorites is linear and again points towards the origin. We note that the sample suite of Abdelnasser and Kumral (2016) does not include samples from this population of distinctive diorites and also that their trace element data appear seriously scattered and contaminated in many cases.

We modelled the deviations from the liquid line of descent by simple binary mixing between a selected liquid and An_{60} plagioclase. For the linear trends through the gabbros, we chose the point along the liquid line of descent at 11.75 wt% MgO, essentially identical to gabbronorite sample AT40. For the linear trends through the diorites, we chose the point along the liquid line of descent at 8% MgO, similar to diorite sample AT37. The plagioclase component was chosen to fit the intercepts of the mixing lines in CaO, Na_2O and Al_2O_3, but it is also nearly coincident with the most evolved plagioclase predicted to crystallize in the suite. Hence the trace element content of the admixed plagioclase is determined by equilibrium with an evolved liquid found further down the liquid line of descent at 911°C (with 58 wt% SiO_2) and the same partition coefficients used to model the trace element evolution (Supplementary Table 7 also shows the mixing model

construction and results). However, it is not necessary that the admixed plagioclase in fact be cognate to the Atud suite; it could be a crustal contaminant, in which case its trace elements could be decoupled from those fixed by the Atud fractionation trend and it could also have exotic isotopic composition. The constrained version of the model, with cognate plagioclase, however, is especially effective at explaining the TiO_2, Al_2O_3, Fe_2O_3*, CaO and Na_2O variation diagrams as well as the marked difference in enrichment in K_2O and incompatible elements and the contrary behaviour of Sr compared with other trace elements. We note that only Sr is compatible in An_{60} plagioclase; although Ba and Eu partition into plagioclase to some extent their partition coefficients remain less than unity and so these elements are more enriched in the quartz diorite quenched liquid compositions than in the plagioclase-accumulated diorite samples.

The magmatic relationship between gabbronorite and diorite is unclear (geochronological results overlap within uncertainty) but the greater alteration of the diorites suggests that they were present as magmatic mush when the gabbronorite magma was emplaced. On the other hand, diorites contain relicts of gabbroic plagioclase and clinopyroxene, suggesting that gabbronorite may have somehow been transformed by fluids and melts in the MASH zone into diorite. We infer that Atud diorites are part of a larger dioritic MED that formed as a deep crustal mush into which new pulses of mafic magma were periodically emplaced and incorporated. This MASH zone was sustained by the periodic addition of new mafic magma generated by hydrous partial melting of the mantle wedge above a subduction zone. This scenario is shown schematically in Figure 13, although the subduction zone is not shown.

Recognition of the Atud complex as part of a Cryogenian MASH zone may provide some new insights into gold mineralization in the region. Several shafts in the diorite on the east side of the complex show where the mineralization is concentrated. Gold is associated with a NNW-trending zone of strongly sericitized and silicified diorite. The precise relationship of gold mineralization and magmatism at Gebel Atud requires further study.

Conclusions

Hornblende-bearing gabbroic and dioritic rocks from the Atud igneous complex in the Eastern Desert of Egypt provide new insights into how juvenile continental crust of the Arabian–Nubian Shield formed in Cryogenian time. Olivine gabbronorites, diorites and quartz diorites are the same age (*c*. 695 Ma), and mafic parental magmas were derived by hydrous partial melting of subduction-modified mantle. These magmas evolved further in a deep crust MASH zone where they fractionated to form diorites and quartz diorites. Magmatic evolution was accompanied by negligible to minor contributions from older continental crust. This lower crust was uplifted and exposed as a result of younger (probably Ediacaran) tectonic movements.

The Atud igneous complex is part of a large swath of mafic–intermediate magmatic rocks known as the metagabbro–epidiorite–diorite (MED) complex that crops out extensively in the region. We suspect that MED rocks formed around the same time as lower crust beneath a long-lived (*c*. 60 myr) convergent margin. Atud complex igneous rocks and correlatives in the MED formed as a deep crustal mush into which new pulses of mafic magma were periodically emplaced and incorporated. This MASH zone was sustained by the periodic addition of new mafic magma generated by hydrous partial melting of the mantle wedge above a subduction zone. The upper crust associated with this Cryogenian convergent margin may be preserved as gneisses of the Hafafit complex to the south, but further work will be needed to define what if any relationship the Atud complex has with other MED rocks as well as what is the relationship between Atud and MED on the one hand and Hafafit gneisses on the other hand.

Acknowledgements We appreciate thoughtful and constructive reviews by J.-P. Liégeois and R. A. Terentiev. K. Lindén and H. Jeon are thanked for assistance with the SIMS analyses. The Nordsim laboratory operates as a Swedish Research Council infrastructure under grant 2017-00671; this is Nordsim contribution 639. This is UTD Geosciences contribution number 1353.

Funding This work was funded by the Directorate for Geosciences (OCE-1826310).

Author contributions **RS**: conceptualization (lead), formal analysis (lead), visualization (lead), writing – original draft (lead), writing – review & editing (lead); **KA**: investigation (supporting), visualization (supporting), writing – review & editing (supporting); **PA**: formal analysis (supporting), writing – original draft (supporting); **MA**: investigation (supporting), writing – original draft (supporting), writing – review & editing (supporting); **MIL**: investigation (supporting), visualization (supporting), writing – original draft (supporting), writing – review & editing (supporting); **HSM**: investigation (supporting), writing – original draft (supporting); **MR**: investigation (supporting), visualization (supporting), writing – original draft (supporting); **RLR**: investigation (equal), visualization (equal), writing – review & editing (equal); **MW**: investigation (equal), visualization (equal), writing – review & editing (equal).

Data availability statement All data generated or analysed during this study are included in this published article (and its supplementary information files).

Scientific editing by Igor Villa

References

Abdelnasser, A. and Kumral, M. 2016. Mineral chemistry and geochemical behavior of hydrothermal alterations associated with mafic intrusive-related Au deposits at the Atud area, Central Eastern Desert, Egypt. *Ore Geology Reviews*, **77**, 1–24, https://doi.org/10.1016/j.oregeorev.2016.01.011

Abdelnasser, A. and Kumral, M. 2017. The nature of gold-bearing fluids in Atud gold deposit, central Eastern Desert, Egypt. *International Geology Review*, **59**, 1845–1860, https://doi.org/10.1080/00206814.2017.1299043

Akaad, M.K. and Essawy, M. 1964. The Metagabbro–Diorite Complex, N.E. of Gabal Atud, Eastern Desert, and the term 'Epidiorite'. *Bulletin of Science and Technology, Assiut University*, **7**, 83–104.

Ali, K.A., Stern, R.J., Manton, W.I., Kimura, J.-I. and Khamis, H.A. 2009. Geochemistry, Nd isotopes, and U–Pb SHRIMP zircon dating of Neoproterozoic volcanic rocks from the Central Eastern Desert of Egypt: New insights into the ~750 Ma crust-forming event. *Precambrian Research*, **171**, 1–22, https://doi.org/10.1016/j.precamres.2009.03.002

Ali, K.A., Stern, R.J., Manton, W.I., Johnson, P.R. and Mukherjee, S.K. 2010. Neoproterozoic diamictite in the Eastern Desert of Egypt and Northern Saudi Arabia: Evidence of ~750 Ma glaciation in the Arabian–Nubian Shield. *International Journal of Earth Sciences*, **90**, 705–726, https://doi.org/10.1007/s00531-009-0427-3

Andersen, D.J., Lindsley, D. and Davidson, P.M. 1993. QUILF: A PASCAL program to assess equilibria among Fe–Mg–Mn–Ti oxides, pyroxenes, olivine, and quartz. *Computers and Geosciences*, **19**, 1333–1350, https://doi.org/10.1016/0098-3004(93)90033-2

Annen, C., Blundy, J.D. and Sparks, R.S.J. 2006. The genesis of intermediate and silicic magmas in deep crustal hot zones. *Journal of Petrology*, **47**, 505–539, https://doi.org/10.1093/petrology/egi084

Augland, L.E., Andresen, A. and Boghdady, G.Y. 2012. U–Pb ID-TIMS dating of igneous and metaigneous rocks from the El-Sibai area: Time constraints on the tectonic evolution of the Central Eastern Desert, Egypt. *International Journal of Earth Science*, **101**, 25–37, https://doi.org/10.1007/s00531-011-0653-3

Bea, F. 2012. The sources of energy for crustal melting and the geochemistry of heat-producing elements. *Lithos*, **153**, 278–291, https://doi.org/10.1016/j.lithos.2012.01.017

Be'eri-Shlevin, Y., Katzir, Y. and Valley, J.W. 2009. Crustal evolution and recycling in a juvenile continent: oxygen isotope ratio of zircon in the northern Arabian Nubian Shield. *Lithos*, **107**, 169–184, https://doi.org/10.1016/j.lithos.2008.10.001

Be'eri-Shlevin, Y., Katzir, Y., Blichert-Toft, J., Kleinhanns, I.C. and Whitehouse, M. 2010. Nd–Sr–Hf–O isotope provinciality in northernmost Arabian–Nubian Shield: Implication for crustal evolution. *Contributions to Mineralogy and Petrology*, **160**, 181–201, https://doi.org/10.1007/s00410-009-0472-8

Bianchini, G., Bryce, J.G., Blichert-Toft, J., Beccaluva, L. and Natali, C. 2014. Mantle dynamics and secular variations beneath the East African Rift: insights from peridotite xenoliths (Mega, Ethiopia). *Chemical Geology*, **386**, 49–58, https://doi.org/10.1016/j.chemgeo.2014.07.024

Brey, G.P. and Köhler, T. 1990. Geothermobarometry in four-phase lherzolites II. New thermobarometers, and practical assessment of existing thermobarometers. *Journal of Petrology*, **31**, 1353–1378, https://doi.org/10.1093/petrology/31.6.1353

Condie, K.C. 1999. Mafic crustal xenoliths and the origin of the lower continental crust. *Lithos*, **46**, 95–101, https://doi.org/10.1016/S0024-4937(98)00056-5

DePaolo, D.J. 1981. Neodymium isotopes in the Colorado Front Range and crust–mantle interactions in the Proterozoic. *Nature*, **291**, 193–196, https://doi.org/10.1038/291193a0

El Ramly, M.F. 1972. A New Geological Map for the Basement Rocks in the Eastern and South-western Deserts of Egypt. Scale 1:1,000,000. *Annals of the Geological Survey of Egypt*, **2**, 1–18.

Engel, A.E.J., Dixon, T.H. and Stern, R.J. 1980. Late Precambrian evolution of Afro-Arabian crust from ocean-arc to craton. *Geological Society of America Bulletin*, **91**, 699–706, https://doi.org/10.1130/0016-7606(1980)91<699:LPEOAC>2.0.CO;2

General Petroleum Corporation. 1987. *Quseir quadrangle NG 36 NE and Gabal Hamata quadrangle NG 36 SE*. General Petroleum Corporation, Cairo, Egypt.

Ghoneim, M.F. 1989. Mineral chemistry of some gabbroic rocks of the Central Eastern Desert, Egypt. *Journal of African Earth Sciences*, **9**, 389–295, https://doi.org/10.1016/0899-5362(89)90071-7

Goldstein, S.L., O'Nions, R.K. and Hamilton, P.J. 1984. A Sm–Nd isotopic study of atmospheric dusts and particulates from major river systems. *Earth and Planetary Science Letters*, **70**, 221–236, https://doi.org/10.1016/0012-821X(84)90007-4

Gualda, G.A.R., Ghiorso, M.S., Lemons, R.V. and Carley, T.L. 2012. Rhyolite-MELTS: A Modified Calibration of MELTS Optimized for Silica-Rich, Fluid-Bearing Magmatic Systems. *Journal of Petrology*, **53**, 875–890, https://doi.org/10.1093/petrology/egr080

Hagag, W., Moustafa, R. and Hamimi, Z. 2018. Neoproterozoic Evolution and Najd Related Transpressive Shear Deformations along Nugrus Shear Zone, South Eastern Desert, Egypt (Implications from Field-Structural Data and AMS-Technique). *Geotectonics*, **52**, 114–133, https://doi.org/10.1134/S0016852118010077

Hildreth, W. and Moorbath, S. 1988. Crustal contributions to arc magmatism in the Andes of Central Chile. *Contributions to Mineralogy and Petrology*, **98**, 455–489, https://doi.org/10.1007/BF00372365

Irvine, T.N. and Baragar, W.R.A. 1971. A guide to the chemical classification of the common volcanic rocks. *Canadian Journal of Earth Sciences*, **8**, 523–545, https://doi.org/10.1139/e71-055

Jarrar, G.H., Theye, T., Yaseen, N., Whitehouse, M., Pease, V. and Passchier, C. 2013. Geochemistry and *P–T–t* evolution of the Abu-Barqa Metamorphic Suite, SW Jordan, and implications for the tectonics of the northern Arabian–Nubian Shield. *Precambrian Research*, **239**, 56–78, https://doi.org/10.1016/j.precamres.2013.08.003

Kröner, A., Krüger, J. and Rashwan, A.A.A. 1994. Age and tectonic setting of granitoid gneisses in the Eastern Desert of Egypt and south-west Sinai. *Geologische Rundschau*, **83**, 502–513, https://doi.org/10.1007/BF01083223

Laube, N. and Springer, J. 1998. Crustal melting by ponding of mafic magmas: A numerical model. *Journal of Volcanology and Geothermal Research*, **81**, 19–35, https://doi.org/10.1016/S0377-0273(97)00072-3

Liu, J. and Zhang, L. 2013. Neoproterozoic low to negative $\delta^{18}O$ volcanic and intrusive rocks in the Qinling Mountains and their geological significance. *Precambrian Research*, **230**, 138–167, https://doi.org/10.1016/j.precamres.2013.02.006

Ludwig, K.R. 2001. *Users Manual for Isoplot/Ex version 2.05*. Berkeley Geochronology Center, Special Publication, **1a**.

Meshesha, D., Shinjo, R., Matsumura, R. and Chekol, T. 2011. Metasomatized lithospheric mantle beneath Turkana depression in southern Ethiopia (the East Africa rift): Geochemical and Sr–Nd–Pb isotopic characteristics. *Contributions to Mineralogy and Petrology*, **162**, 889–907, https://doi.org/10.1007/s00410-011-0630-7

Mutch, E.J.F., Blundy, J.D., Tattitch, B.C., Cooper, F.J. and Brooker, R.A. 2016. An experimental study of amphibole stability in low-pressure granitic magmas and a revised Al-in-hornblende geobarometer. *Contributions to Mineralogy and Petrology*, **171**, 2–27, https://doi.org/10.1007/s00410-015-1215-7

Powell, J.H., Abed, A. and Jarrar, G. 2015. Ediacaran Araba Complex of Jordan. *GeoArabia*, **20**, 99–156.

Putirka, K.D. 2008. Thermometers and Barometers for Volcanic Systems. *In*: Putirka, K.D. and Tepley, F.J., III (eds) *Minerals, Inclusions and Volcanic Processes*. Mineralogical Society of America and Geochemical Society, Reviews in Mineralogy and Geochemistry, **69**, 61–120, https://doi.org/10.2138/rmg.2008.69.3

Roeder, P.L. and Emslie, R.F. 1970. Olivine–liquid equilibrium. *Contributions to Mineralogy and Petrology*, **29**, 275–289, https://doi.org/10.1007/BF00371276

Smith, P.M. and Asimow, P.D. 2005. Adiabat_1ph: A New Public Front-End to the MELTS, PMELTS, and PHMELTS Models. *Geochemistry, Geophysics, Geosystems*, **6**, Q02004, https://doi.org/10.1029/2004GC000816

Stern, R.J. 2017. Neoproterozoic formation and evolution of Eastern Desert continental crust – The importance of the infrastructure–superstructure transition. *Journal of African Earth Sciences*, **146**, 15–27, https://doi.org/10.1016/j.jafrearsci.2017.01.001

Stern, R.J. and Ali, K. 2020. Crustal evolution of the Egyptian Precambrian rocks. *In*: Hamimi, Z., El-Barkooky, A., Martínez Frías, J., Fritz, H. and Abd El-Rahman, Y. (eds) *Geology of Egypt*. Regional Geology Reviews, Springer Nature Switzerland, 131–151. https://doi.org/10.1007/978-3-030-15265-9_2

Stern, R.J. and Hedge, C.E. 1985. Geochronologic constraints on late Precambrian crustal evolution in the Eastern Desert of Egypt. *American Journal of Science*, **285**, 97–127, https://doi.org/10.2475/ajs.285.2.97

Streckeisen, A. 1976. To each plutonic rock its proper name. *Earth-Science Reviews*, **12**, 1–33, https://doi.org/10.1016/0012-8252(76)90052-0

Tera, F. and Wasserburg, G.J. 1972. U–Th–Pb systematics in three Apollo 14 basalts and the problem of initial Pb in lunar rocks. *Earth and Planetary Science Letters*, **14**, 281–304, https://doi.org/10.1016/0012-821X(72)90128-8

Valley, J.W. 2003. Oxygen isotopes in zircons. *In*: Hanchar, J.M. and Hoskin, P.W.O. (eds) *Zircon*. Mineralogical Society of America and Geochemical Society, Reviews in Mineralogy and Geochemistry, **53**, 343–385, https://doi.org/10.2113/0530343

Valley, J., Kinny, P., Schulze, D. and Spicuzza, M.J., 1998. Zircon megacrysts from kimberlite: oxygen isotope variability among mantle melts. *Contributions to Mineralogy and Petrology*, **133**, 1–11.

van Schijndel, V., 2013. *Precambrian Crustal Evolution of the Rehoboth, Southern Africa*. PhD thesis, University of Göthenburg.

Wei, C.S., Zheng, Y.F., Zhao, Z.F. and Valley, J.W. 2002. Oxygen and neodymium isotope evidence for recycling of juvenile crust in northeast China. *Geology*, **30**, 375–378, https://doi.org/10.1130/0091-7613(2002)030<0375:OANIEF>2.0.CO;2

Wilson, M. 1989. *Igneous Petrogenesis*. Unwin Hyman, London.

Yaseen, N., Pease, V., Jarrar, G.H. and Whitehouse, M. 2013. U–Pb detrital zircon provenance of the Saramuj Conglomerate, Jordan, and implications for the Neoproterozoic evolution of the Red Sea region. *Precambrian Research*, **239**, 6–23, https://doi.org/10.1016/j.precamres.2013.10.008

Zheng, J.P., Griffin, W.L. *et al.* 2004. 3.6 Ga lower crust in central China: new evidence on the assembly of North China Craton. *Geology*, **32**, 229–232, https://doi.org/10.1130/G20133.1

Zheng, J.P., Griffin, W.L., O'Reilly, S.Y., Zhang, M., Pearson, N.J. and Pan, Y.M. 2006. Widespread Archean basement beneath the Yangtze Craton. *Geology*, **34**, 417–420, https://doi.org/10.1130/G22282.1